

Neutron star collapse and gravitational waves with a non-convex equation of state

Miguel A. Aloy¹, José M. Ibáñez^{1,2}, Nicolas Sanchis-Gual¹, Martin Obergaulinger¹,
José A. Font^{1,2}, Susana Serna³, and Antonio Marquina⁴

¹*Departamento de Astronomía y Astrofísica, Universitat de València, Dr. Moliner 50, 46100, Burjassot (València), Spain*

²*Observatori Astronòmic, Universitat de València, C/ Catedrático José Beltrán 2, 46980, Paterna (València), Spain*

³*Departament de Matemàtiques, Universitat Autònoma de Barcelona, Edifici C, 08193 Bellaterra (Barcelona), Spain*

⁴*Departamento de Matemáticas, Universitat de València, Dr. Moliner 50, 46100, Burjassot (València), Spain*

25 January 2019

ABSTRACT

The thermodynamical properties of the equation of state (EoS) of high-density matter (above nuclear saturation density) and the possible existence of exotic states such as phase transitions from nuclear/hadronic matter into quark-gluon plasma, or the appearance of hyperons, may critically influence the stability and dynamics of compact relativistic stars. From a theoretical point of view, establishing the existence of those states requires the analysis of the “convexity” of the EoS. We show indications of the existence of regions in the dense-matter EoS where the thermodynamics may be non-convex as a result of a non-monotonic dependence of the sound speed with the rest-mass density. When this happens, non-conventional dynamics may develop. In this paper we investigate the effects of a phenomenological, non-convex EoS on the equilibrium structure of stable compact stars and on the dynamics of unstable neutron stars that collapse gravitationally to black holes, both for spherically symmetric and uniformly-rotating configurations. We show how the dynamics of the collapse with a non-convex EoS departs from the convex case, leaving distinctive imprints on the gravitational waveforms. The astrophysical significance of these results for microphysical EoSs is discussed.

Key words: dense matter – equation of state – gravitational waves – hydrodynamics – shock waves – stars: neutron

1 INTRODUCTION

A long-standing, fundamental, and still open issue in relativistic astrophysics is the knowledge of the equation of state (EoS) describing the thermodynamical properties of high-density matter, i.e. matter at densities above nuclear-matter. Such extreme conditions are achieved in the cores of neutron stars. Theoretical progress towards the understanding of this issue relies on electromagnetic observations and heavy-ion experiments (see Glendenning (2000); Heiselberg & Hjorth-Jensen (2000); Glendenning (2001); Weber (2005); Camenzind (2007); Haensel et al. (2007) and references therein). With the recent observations of gravitational waves from mergers of binary black holes and binary neutron stars (Abbott et al. 2016a,b, 2017a,b,c,f,d) a new channel to collect complementary information and improve our understanding of the dense-matter EoS has already opened (see, e.g. the recent constraints obtained in Abbott et al. 2018; Margalit & Metzger 2017; Annala et al. 2018; De et al. 2018; Malik et al. 2018; Most et al. 2018b; Radice et al. 2018; Raithel et al. 2018; Zhou et al. 2018). However, despite the ongoing efforts, the issue has not been fully addressed thus far.

There are many reasons why this matter must be worked out.

First, because the properties of the dense-matter EoS and the possible existence of exotic states such as phase transitions (PTs) to quark-gluon plasma or associated with the presence of hyperons in the core of neutron stars, may critically influence the stability and dynamics of these objects. Furthermore, a third family of compact stars, more compact and denser than neutron stars, and originated by the appearance of quark phases in the core of neutron stars, has been long suggested (Schertler et al. 2000; Glendenning & Kettner 2000). More recently, the observations of two high-mass pulsars, PSR J1614-2230 (Demorest et al. 2010) and PSR J0348-0432 (Antoniadis et al. 2013), has also placed severe constraints on the dense-matter EoS. In particular, the softening of the EoS due to the presence of hyperons or PTs to quark matter or boson condensates is prone to affect the stability of neutron stars (Bednarek et al. 2012; Zdunik & Haensel 2013). The possibility of different types of phases, i.e. neutrons and quarks, coexisting in dense matter is currently under intense scrutiny (see Buballa et al. (2014) and references therein). Moreover, the possible existence of hybrid stars has recently been considered by Bejger et al. (2017).

The dense-matter EoS also plays a fundamental role in the evolution (on a hydrodynamical timescale) of archetypal scenar-

ios of relativistic astrophysics such as core-collapse supernovae, short- and long-duration progenitors of gamma-ray bursts, the cooling of proto-neutron stars, the formation of stellar-mass black holes (BHs), or the merger of compact-binary systems. In particular, and in the context of PTs, the dynamics of neutron star cores collapsing to BHs has been analyzed numerically in spherical symmetry by Abdikamalov et al. (2009) and by Peres et al. (2013a). In the former work the collapse is induced by a PT from hadronic matter to deconfined quark matter, while in the latter the collapse is induced by a PT to hyperonic matter. The corresponding extensions of these works including rotation can be found in Dimmelmeier et al. (2009); Bejger et al. (2012) and Peres (2013).

From a theoretical point of view, the existence of such exotic states of matter in the dense-matter EoS also requires the analysis of the “convexity” of the EoS. Relevant contributions towards the knowledge of the properties of non-convex thermodynamics induced by some EoS were made in the pioneering works of Bethe (1942), Zel’dovich (1946), and Thompson (1971). In particular Thompson (1971) introduced the concept of *fundamental derivative* in gas dynamics. Nowadays, fluids which display a region of negative values of the fundamental derivative are called Bethe-Zel’dovich-Thompson fluids, or BZT fluids (see Voss (2005) and references therein). A classical example is provided by a Van der Waals EoS. In this EoS, besides the mixing regime where different phases coexist, there is a region of non-convexity, where the fundamental derivative is negative (Menikoff & Plohr 1989). BZT fluids have drawn some attention in the last fifteen years due to their potential applications in industry (see, e.g. Cinnella 2008; Guardone et al. 2010). Unlike a regular fluid, a BZT fluid might condense on isentropic compression¹.

The extension to relativistic fluid dynamics of previous studies on BZT fluids in the framework of *classical* fluid dynamics was accomplished by Ibáñez et al. (2013). This work presented the conditions under which the hyperbolic system of relativistic Euler equations is convex. The authors considered a perfect fluid obeying a causal EoS and the results were obtained by analyzing the properties of the characteristic fields of the relativistic hydrodynamics equations. Following Thompson (1971) the conditions were given in terms of the so-called (classical) fundamental derivative, \mathcal{G}_C .

A classical, and somewhat academic, example of a thermodynamical system in which the adiabatic index displays a non-monotonous behaviour with the density is the region around the neutron-drip point in cold catalyzed dense matter (Shapiro & Teukolsky 1983). Similar regions appear also in EoSs derived from a field-theoretical model for nuclear and neutron matter, both at zero temperature (Diaz Alonso 1985) and at finite temperature (Martí et al. 1988). Moreover, the most popular EoSs used in recent hydrodynamical simulations of compact stars display again, in some regions of the space of thermodynamical parameters, a non-monotonous behaviour of the adiabatic exponent with the density (as can be seen in the fittings reported by Haensel et al. 2002; Haensel & Potekhin 2004; Haensel et al. 2007; Bauswein et al. 2010). Those regions are good candidates to develop non-convex thermodynamics.

Other examples can be found at densities much higher than nu-

clear saturation density ($n_0 \approx 0.16 \text{ fm}^{-3}$) at which nuclear/hadronic matter undergoes a transition into a quark-gluon plasma (QGP). The nature of the finite-temperature QCD transition remains ambiguous (Aoki et al. 2006) and may even evolve from a crossover transition at low baryon number density to a first-order PT at high baryon number density with the existence of a critical point. Using QCD lattice techniques, the HotQCD Collaboration (Bazavov et al. 2014) and the Wuppertal-Budapest Collaboration (Borsányi et al. 2014), have reported results about the EoS characterizing the transition from the hadronic phase into the QGP phase. Their results, which favor the crossover nature of the transition, in the continuum extrapolated EoS and in the phenomenologically relevant range of temperature, 130 – 400 MeV, show similarities regarding the trace anomaly, pressure, energy density and entropy density. The energy density in the crossover region, $145 \leq T \text{ (MeV)} \leq 163$, is a factor of about 1.2 to 3.1 times the energy density at nuclear saturation density, and the sound speed has a minimum $\simeq 0.38$ (Bazavov et al. 2014) within the former interval. Following a different strategy, which combines the knowledge of the EoS of hadronic matter at low densities with the observational constraints on the masses of neutron stars, Bedaque & Steiner (2015) conclude that the speed of sound of dense matter is not a monotonous function of the energy density, with local maximum and minimum above and below $1/\sqrt{3}$, respectively. As we show in Sec. 3, a non-convex region in the space of thermodynamical parameters appears where the adiabatic index is an strong enough decreasing function of the density. This is equivalent to demanding that the classical local sound speed be a sufficiently steep decreasing function of the density. Roughly, regions where the sound speed is not a monotonic function of the density are suitable to develop a non-convex thermodynamics. Indeed, as we shall see in this paper, these regions may also develop a distinctive hydrodynamic behaviour in the course of the collapse of unstable neutron star-like configurations.

Motivated by the above indications of the existence of possible regions in the dense-matter EoS where the thermodynamics can be non-convex, we present in this paper a numerical study of the structure and dynamics of compact stellar configurations described by a BZT fluid. We choose a particularly simple form of the EoS, namely an ideal gas EoS with an adiabatic index which depends on the density (Ibáñez et al. 2018). While this phenomenological EoS can only be regarded as a *toy-model*, it serves nonetheless to exemplify the particularities that appear when the EoS is non-convex. For our study we consider two different situations, firstly, the equilibrium structure of stable compact stars and, secondly, the dynamics of unstable neutron stars that collapse gravitationally to BHs, both for spherically symmetric and uniformly-rotating initial configurations. A future study using actual microphysical EoS from nuclear physics will be presented elsewhere.

This paper is organized as follows: Section 2 shows that non-convex thermodynamics may exist in various microphysical EoS of common use in astrophysical scenarios such as massive stellar core collapse. In most cases, this convexity loss is associated to the existence of first-order PTs. Section 3 describes our toy-model, non-convex EoS. This EoS is employed to obtain the results presented in the following three sections. Section 4 discusses the structure of spherically-symmetric relativistic stellar equilibrium configurations, while Sections 5 and 6 analyse the dynamics of unstable configurations which promptly collapse producing a central BH in spherical and axial symmetry, respectively. Since, as we show below, the effects of convexity loss are bound to very compact collapsing cores, the observational signature of this *anomalous* thermodynamics may potentially be best noticed on the gravitational-

¹ As a side remark, we point out that BZT flows may show a non-convex dynamics in which compound waves as, for example, rarefaction shocks, can develop during their evolution (see Argrow 1996; Guardone & Vigeveno 2002; Voss 2005; Cinnella & Corre 2006; Serna & Marquina 2014).

wave signature. Thus, from the collapsing, axisymmetric, rotating cores we present in Section 6, we calculate their gravitational-wave emission aiming at identifying features that differentiate convex dynamics from non-convex ones. Finally, the conclusions of our work are presented in Section 7.

2 NON-CONVEXITY IN MICROPHYSICAL EOS EMPLOYED IN STELLAR CORE COLLAPSE

In classical fluid dynamics, the convexity of a thermodynamical system is determined by the EoS (Menikoff & Plohr 1989) and, more specifically, by the so-called *fundamental derivative*, $\mathcal{G}_{(C)}$

$$\mathcal{G}_{(C)} := -\frac{1}{2}V \frac{\frac{\partial^2 p}{\partial V^2} \Big|_s}{\frac{\partial p}{\partial V} \Big|_s}, \quad (1)$$

where $V := 1/\rho$ the specific volume, ρ the rest mass density, p the pressure and s is the specific entropy. The fundamental derivative measures the convexity of the isentropes in the $p-V$ plane. If $\mathcal{G}_{(C)} > 0$ then the isentropes in the $p-V$ plane are convex and the rarefaction waves are expansive.

The relationship between the classical and the relativistic fundamental derivatives was found in Ibáñez et al. (2013) and is given by

$$\mathcal{G}_{(R)} = \mathcal{G}_{(C)} - \frac{3}{2}c_{s(R)}^2, \quad (2)$$

where $c_{s(R)}$ is the relativistic sound speed, related to the classical definition of the sound speed,

$$c_{s(C)}^2 = \frac{\partial p}{\partial \rho} \Big|_s, \quad (3)$$

through the relation $c_{s(C)}^2 = hc_{s(R)}^2$, where $h = 1 + \varepsilon + p/\rho$ is the specific enthalpy and ε the specific energy.

Equation (1) can be cast in two different forms (Menikoff & Plohr 1989, see also Ibáñez et al. 2018) which are useful to understand the physical origin of the sign of the fundamental derivative (i.e. the root of the convexity loss). In terms of the adiabatic index, Γ_1 ,

$$\Gamma_1 := \frac{\partial \ln p}{\partial \ln \rho} \Big|_s = \frac{\rho}{p} c_{s(C)}^2 \quad (4)$$

and its density derivatives (at constant entropy) one finds

$$\mathcal{G}_{(C)} = \frac{1}{2} \left(1 + \Gamma_1 + \frac{\partial \ln \Gamma_1}{\partial \ln \rho} \Big|_s \right), \quad (5)$$

and in terms of the derivatives of the sound speed

$$\mathcal{G}_{(C)} = 1 + \frac{\partial \ln c_{s(C)}}{\partial \ln \rho} \Big|_s. \quad (6)$$

Thus, it is clear that a necessary condition for the fundamental derivative to be negative is that $\partial \Gamma_1 / \partial \rho \Big|_s < 0$. Alternatively, it is sufficient for $\mathcal{G}_{(C)} < 0$ that $\partial \ln c_{s(C)} / \partial \ln \rho \Big|_s < -1$.

We remind the reader that thermodynamics places no constraint on the sign of the fundamental derivative (Menikoff & Plohr 1989). A system with a negative fundamental derivative may be thermodynamically stable as long as $\Gamma_1 \geq 0$, which implies that the energy per unit mass remains strictly convex (as a function of V) along an isentrope.

2.1 Sample of microphysical EoS

We have performed a survey of a few nuclear-matter EoS which can be found in the Compstar Online Supernovae Equations of State (CompOSE)² looking for regions of the parameter space in which either the relativistic or the classical fundamental derivative become negative. We do not aim to exhaustively check all the possible dense-matter EoSs. Instead, we shall see that some of the EoSs we consider here (all of which have been used in the context of stellar core collapse) display regions where the thermodynamics is potentially non-convex. The EoS from the CompOSE database have been included to sample cases in which baryons are treated as non-relativistic particles or, alternatively, they are included within a suitable relativistic theory. Also, we have considered variants of the latter cases where different parameter sets of a relativistic mean-field (RMF) theory are available and employed in astrophysical simulations. Finally, different variants of the EoS account for the possibility of transitions to quark matter or include more exotic particles such as hyperons. We note that the tables employed to compute the fundamental derivatives are evaluated at exactly the same values of the baryon number density, n , and charge fraction $Y_q = n_q/n$ (n_q is the charge density of strongly interacting particles) as in the CompOSE database. This is an important point, since high-order derivatives of the thermodynamic variables (like those needed for the calculation of the fundamental derivatives) may display small amplitude, high-frequency oscillations associated to the discretization of the EoS table. While this problem is minor in regions where the relativistic fundamental derivative is positive and significantly different from zero, it may affect the determination of a “physically sound” non-convex region when the fundamental derivatives are close to zero. We warn the reader on the “numerical” loss of convexity associated to insufficiently fine thermodynamic discretization of some tabulated EoS when the adiabatic index is non-constant (Vaidya et al. 2015).³

The EoS of Lattimer & Swesty (1991) with compression modulus $K = 220$ MeV (LS220) is considered here in two variants: LS220 and LS220 (Λ). The difference between both cases is the introduction of Λ -hyperons in the second one (following Oertel et al. 2012; Gulminelli et al. 2013). The hyperon-nucleon interaction is taken from the model by Balberg & Gal (1997). The Lattimer & Swesty (1991) EoS assumes that the nuclear interaction is an effective non-relativistic Skyrme type model without momentum dependence. Nucleons are treated as non-relativistic particles; α -particles as hard spheres forming an ideal Boltzmann gas. As the density increases, nuclei dissolve into homogeneous nuclear matter above saturation density. The (assumed first-order) PT to bulk nuclear matter is treated by a Maxwell construction. Photons and electrons/positrons are included as a free gas. The low density extension, below the validity range of the original Lattimer and Swesty EoS is based on a nuclear statistical equilibrium model by Oertel et al. (2012). A first application of this EoS in the supernova context is described in Peres et al. (2013b). As for the LS220 (Λ) EoS, it has been broadly employed in the literature (e.g. Obergaulinger et al. 2014; Obergaulinger & Aloy 2017).

The EoS of Shen et al. (1998a,b) (dubbed STOS, hereafter)

² <http://compose.obspm.fr>

³ As a technical note, we point out that to reduce the numerical noise in the evaluation of the fundamental derivatives we tabulate the EoS as a function of n , of Y_q and of the entropy per baryon, s , using the CompOSE public software. This is specially useful since we make use of derivatives at constant entropy in the expressions of $\mathcal{G}_{(C)}$ (Eq. (6); below) and $\mathcal{G}_{(R)}$ (Eq. (2)).

uses the Thomas-Fermi and variational approximations with a RMF model. It has been considered here in two variants. The first one STOS, with only baryonic contributions (no leptons or photons included). The second variant of the Shen et al. EoS, STOS (B165), includes a transition to quark matter (Sagert et al. 2009, 2010; Fischer et al. 2011). The transition from the hadronic to the quark phase is done via a Gibbs construction (as in Drago & Tambini 1999; Nakazato et al. 2008) and employing a bag model for the quark phase with a bag constant of $B^{1/4} = 165 \text{ MeV}$ and a strong interaction constant (Alford et al. 2007) $\alpha_s = 0.3$. In both cases the EoS employs a non-linear RMF model with the TM1 parametrization (Sugahara & Toki 1994) of the effective interaction. Only neutrons, protons, alpha particles and a single heavy nucleus as well as electrons/positrons and photons are considered. The STOS (B165) EoS yields a maximum gravitational mass of $1.67M_\odot$ (Sagert et al. 2010) and, therefore, it is not compatible with the maximum masses observed for neutron stars. However, this EoS received some attention in the past decade since it may leave an effect on the supernova explosion mechanism due to the formation of a secondary shock wave induced by the QGP PT (Sagert et al. 2009).⁴ The high degree of isospin asymmetry and the presence of temperatures of a few MeV in the early post-bounce phase of core collapse may induce the transition to the quark phase already around the saturation number density.

We have also included cases in which the hadronic EoS is based on the statistical model of Hempel & Schaffner-Bielich (2010) (HS) and with RMF interactions of different types. These are the EoS tagged with BHB ($\Lambda\phi$), HS (DD2Y), HS (TMA), HS (TM1), HS (NL3), SFHO, SFHX. The first and second ones, BHB ($\Lambda\phi$) (Banik et al. 2014) and HS (DD2Y) (Marques et al. 2017), assume RMF interactions DD2 (Typel et al. 2010), and include Λ -hyperons interacting via ϕ mesons, neutrons, anti-neutrons, protons, anti-protons, lambdas, anti-lambdas, and nuclei. The EoS tagged with HS (TMA), HS (TM1), HS (NL3), SFHO, and SFHX include RMF interactions with parameterizations TMA (Toki et al. 1995), TM1 (Sugahara & Toki 1994), NL3 (Lalazisis et al. 1997), SHFo (Hempel & Schaffner-Bielich 2010) and SFHX (Hempel & Schaffner-Bielich 2010), respectively, and contributions from neutrons, anti-neutrons, protons, anti-protons, electrons, positrons, photons, and nuclei. Applications of HS EoS for various different RMF interactions in supernova simulations can be found in Hempel et al. (2012) and Steiner et al. (2012).

The EoS of Shen et al. (2011a), to which we will refer as GSHen in the following, is based on a RMF model to self-consistently calculate non-uniform matter at intermediate density and uniform matter at high density. At low densities, a virial expansion for a non-ideal gas of nucleons and nuclei is used to obtain the EoS. Three variants of the GSHen EoS are included in our sample: GSHen (FSU1), GSHen (FSU2) and GSHen (NL3). The differences between them are due to the distinct approximations employed within the RMF model. They employ either the FSUGold (FSU1; Todd-Rutel & Piekarewicz 2005) or FSU2 parameters sets of Shen et al. (2011b), in the first two cases, or the NL3 parameter set of Lalazisis et al. (1997).

The SU(3) Chiral Mean Field EoS (CMF; Dexheimer & Schramm 2008; Schürhoff et al. 2010; Dexheimer et al. 2015) is a non-linear realization of the sigma model which includes pseudo-scalar mesons as the angular parameters for the chiral transforma-

tion. In the particular variant of this EoS we have chosen, CMF (Λ), it includes nucleons and hyperons as degrees of freedom (and in the case we consider here also free leptons). Within the model, baryons are mediated by vector-isoscalar, vector-isovector, scalar-isoscalar, and scalar-isovector mesons (including strange quark-antiquark states). We have also considered a variant of the previous EoS that includes also quarks, tagged with CMF (ΛB), which has been recently applied in numerical simulations of mergers of binary neutron stars (Most et al. 2018a).

2.2 Study of the non-convexity

2.2.1 Non-convexity at phase transitions

The nature of PTs taking place under the conditions met in the collapse of massive stellar cores has elicited a long debate in the scientific community (see, e.g. Hempel et al. 2013, and references therein). Following the nomenclature of Iosilevskiy (2010), first-order PTs in nuclear matter are “non congruential” (NCPT), since they involve the coexistence of two or more macroscopic phases with different chemical composition. For instance, in the hadron-quark transition, there can be different types of quarks (see, e.g. Nakazato et al. 2008). The previous property contrasts with the “congruential” nature of first-order PTs in pure substances (e.g. the vapour-liquid PT in water) and introduces additional degrees of freedom, which modify their thermodynamic properties. A very remarkable feature of NCPTs is that they are not isobaric for a fixed temperature, i.e. they happen for a range of pressures corresponding to the range of local concentrations of species involved in the system (c.f. Hempel et al. 2013). It is also known that an NCPT may be “forced-congruential” by assuming, e.g. local charge neutrality in each phase of the coexistence regime independently (Iosilevskiy 2010), in which case the thermodynamics is akin to congruential first-order PTs.

Let us examine the impact on the fundamental derivative of undergoing a first-order PT. Very generally, away from PTs (regardless of whether they are first-order or continuous), $\Gamma_1 > 1$ and displays a slow variation along isentropes ($|\partial \ln \Gamma_1 / \partial \ln \rho|_s \ll 1$), so $\mathcal{G}_{(C)} > 1$ according to Eq. (5). This situation may qualitatively change near congruential or forced-congruential first-order PTs, where $\mathcal{G}_{(C)}$ can be negative (e.g. Menikoff & Plohr 1989), since the sound speed in a mixed-phase is smaller than in a pure phase under the assumption of mechanical equilibrium.⁵ By definition (see, e.g. Callen 1985, ch. 9), in a first-order PT the entropy and the volume are discontinuous, while both the Gibbs and the Helmholtz free energies as well as the pressure are continuous, but not their first derivatives with respect, e.g. temperature or density (more precisely, along coexistence curves the free energies suffer jump discontinuities in their derivatives). Correspondingly, isentropes exhibit kinks across the coexistence curves that translate into jumps of both the sound speed and the adiabatic index (see, e.g. Fig. 7 in Menikoff & Plohr 1989). The jump in any of these two quantities entails a δ -function singularity in $\mathcal{G}_{(C)}$ (see Eqs.(5) or (6)). The coefficient of the δ -function is negative (and thus, $\mathcal{G}_{(C)} < 0$) if the sound speed decreases with density when crossing from a pure to a mixed phase, and positive (i.e. $\mathcal{G}_{(C)} > 0$) otherwise. The former case corresponds to a retrograde saturation boundary, while

⁴ Recently, Fischer et al. (2018) has shown that the transition to the QGP phase may be the engine of supernova explosions in blue supergiants.

⁵ However, these assumptions may break down if the transition between two phases is not instantaneous, so that the system may be out of equilibrium during the PT (c.f. Menikoff & Plohr 1989).

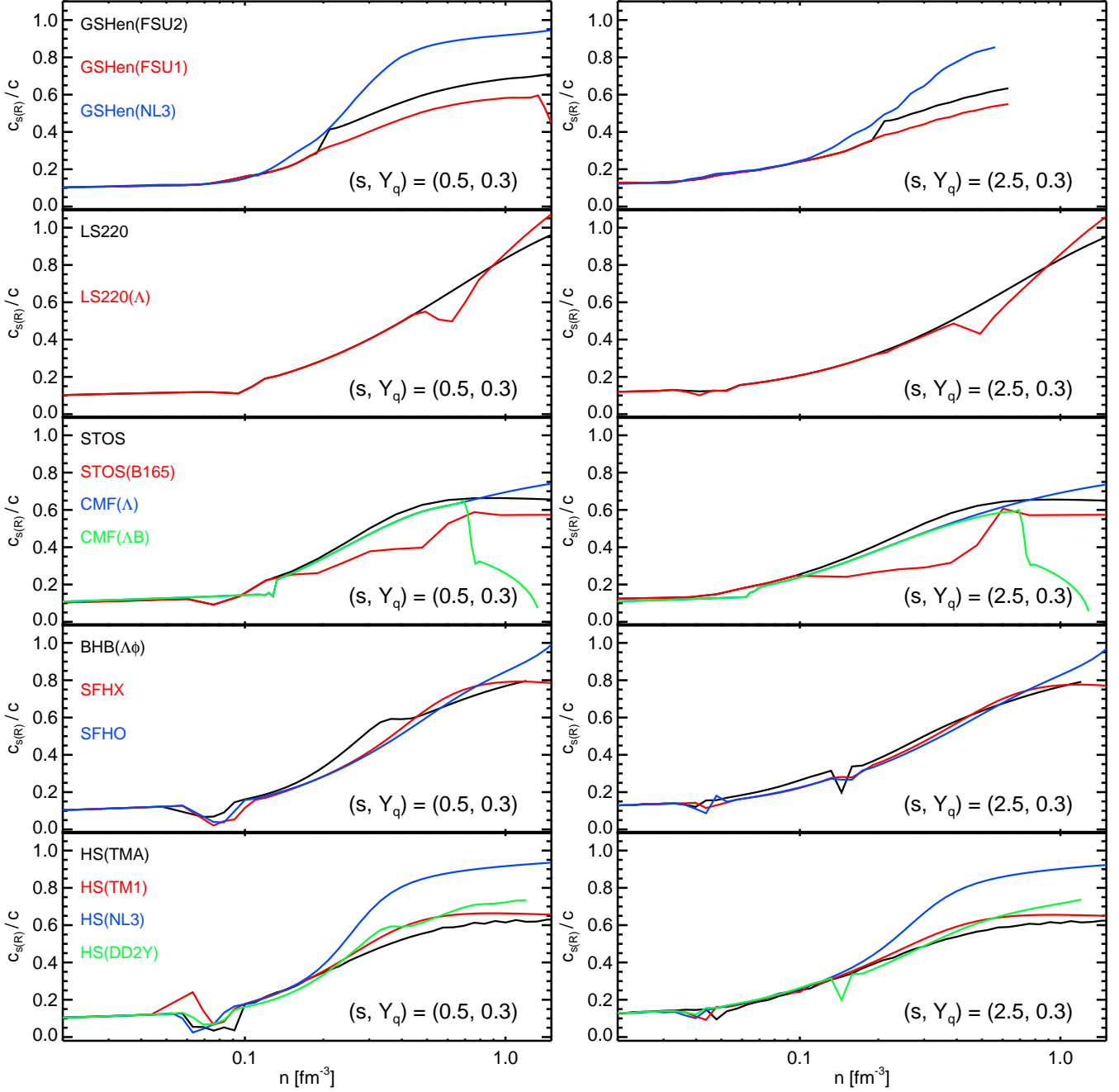


Figure 1. Relativistic sound speed for various nuclear matter EoSs as a function of the baryon number density computed for a fixed value $Y_q = 0.3$ along the isentropes $s = 0.5$ (left panels) and $s = 2.5$ (right panels). The legends GSHen (FSU1), GSHen (FSU2), GSHen (NL3) refer to the GSHen EoS (Shen et al. 2011a) including different parameterizations of the RMF. Models dubbed with LS220 (Δ) and LS220 correspond to the LS220 EoS (Lattimer & Swesty 1991) including hyperons or not including them, respectively. The tags STOS and STOS (B165), refer to the STOS EoS (Shen et al. 1998a,b), the latter one including a transition to a quark matter. BHB ($\Delta\phi$), HS (TMA), HS (TM1), HS (NL3), HS (DD2Y), SFHO and SFHX correspond to the hadronic EoS based on the HS statistical model and implementing RMF interactions of different types. Finally, CMF (Δ), corresponds to the hadronic CMF model, while CMF (ΔB) corresponds to the same EoS, but including also quarks.

the latter one is said to be a normal boundary in the terminology of Thompson et al. (1986).

We now may extend the arguments of Menikoff & Plohr (1989) to NCPTs. The extra complexity induced by the existence of various phases with several globally conserved, net quantum num-

bers (e.g. baryon number, electric charge, strangeness, etc. see, e.g. Hempel et al. 2013) does not change the fact that, if the PT is of first-order type, by definition, the entropy is discontinuous, i.e. there is a finite latent heat released/absorbed during the transition. Since the discontinuity in the entropy is the source of negative val-

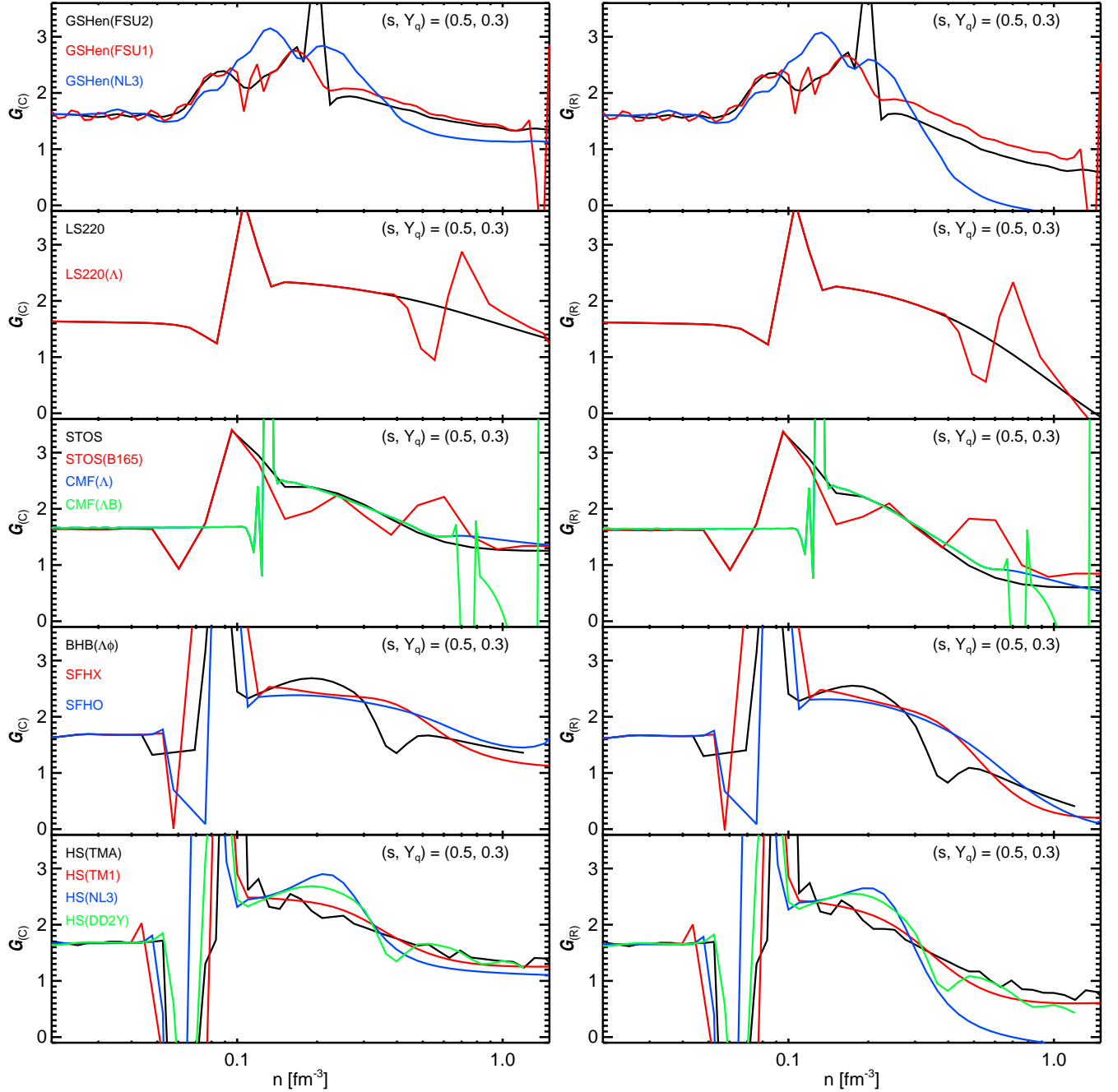


Figure 2. Classical (left) and relativistic (right) fundamental derivative of a few selected dense-matter EoS from ComPOSE as a function of the baryon number density n . For all EoS we fix the value of the entropy per baryon to $s = 0.5$ and of the charge fraction $Y_q = 0.3$.

ues of the fundamental derivative, we shall conclude that the arguments of Menikoff & Plohr (1989) also apply to first-order NCPTs.

2.2.1.1 Transition from inhomogeneous to homogeneous nuclear matter. Applied to the transition from inhomogeneous to homogeneous nuclear matter (happening for $n \lesssim 0.1 \text{ fm}^{-3}$), starting from low number-densities, the sound speed decreases when the homogeneous phase begins to appear in the matter (as can be seen in the bottom panels of Fig. 1), hence marking the location of saturation conditions where $\mathcal{G}_{(C)} < 0$ (i.e. the coexistence bound-

ary is retrograde). Likewise, as the transition to homogeneous matter ends at higher densities, the sound speed increases with density across the coexistence curves and the δ -function singularity in the fundamental derivative yields $\mathcal{G}_{(C)} > 0$ (that is, the coexistence boundary is normal). Obviously, the discrete thermodynamic conditions at which nuclear EoSs are tabulated do not necessarily coincide with the locus of coexistence curves in the phase space. Thus, instead of δ -function discontinuities in $\mathcal{G}_{(C)}$ one produces a smeared transition where the numerically discretized fundamental derivative becomes positive, even if in the continuous case $\mathcal{G}_{(C)} < 0$

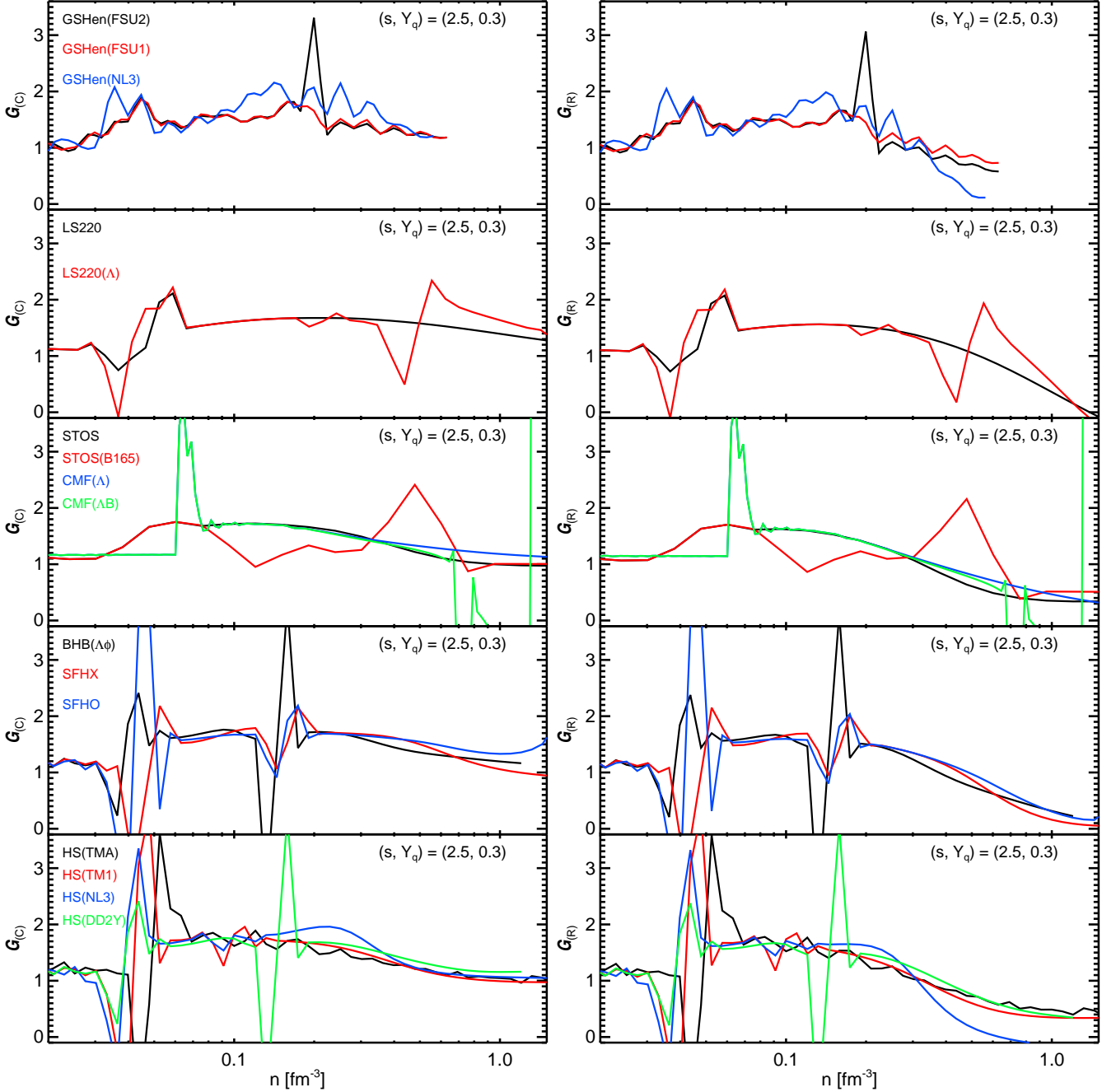


Figure 3. Same as Fig. 2 but computed at an entropy per baryon $s = 2.5$.

along the retrograde coexistence curves. As a consequence, if the PT from inhomogeneous to homogeneous nuclear matter is of first-order kind, we expect that there should be a single point along an isentrope crossing the PT where $\mathcal{G}_{(C)} < 0$ in the continuous limit. Also, due to the tabular nature of the EoSs here considered, it may happen that the spreading of the negative δ -function discontinuity in the fundamental derivative along two or more consecutive tabular values on the same isentrope results in a finite (i.e. not pointwise) number density interval where $\mathcal{G}_{(C)} < 0$. It is also evident that the numerical discretization of derivatives exhibiting jumps across coexistence curves is potentially (very) noisy and, this is the root of

the large oscillations observable in $\mathcal{G}_{(C)}$ and $\mathcal{G}_{(R)}$ in Figs. 2 and 3 (see, especially, the bottom panels of these figures). This considerations lead us to suggest that the tabulation of nuclear matter EoSs should try to adapt to properly capture large gradients in the fundamental derivative, specially when $\mathcal{G}_{(C)}$ becomes negative or approaches zero. In other words, EoS tables should be more densely populated with nodal points near regions where $\mathcal{G}_{(C)} < 0$.

The character of the transition from inhomogeneous to homogeneous nuclear matter (first-order or continuous) is still a matter of debate. Extended (and somewhat controversial) discussions on the treatment of this PT can be found in the literature (e.g. Ducoin

et al. 2007; Raduta & Gulminelli 2010; Pais et al. 2014; Nandi & Schramm 2017), however, we believe that a consensus on the physically soundest assumptions has not been reached in the Nuclear Physics community yet. Furthermore, an insufficiently fine tabulation of an EoS table implementing any Maxwell or Gibbs construction may also result in numerical losses of convexity (see App. A). Hence, we examine the topic of convexity loss bearing this limitation in mind and back up our results by examining the monotony properties of the speed of sound. The previous quantity corresponding to a lower order thermodynamic derivative of the Helmholtz free energy potential than the fundamental derivative and being, hence, less prone to develop spurious numerical oscillations.

Besides the previous considerations, we emphasize that the negative values attained by the classical and relativistic derivatives may result from the treatment of PT in the EoS. Alternative treatments of a PT (corresponding to physically different types of PT) may yield a convex thermodynamic behaviour. For instance, Pons (1999) suggested that employing a Gibbs construction instead of a Maxwell construction in an EoS including hyperons may prevent the formation of discontinuities, keeping finite the compressibility.

We outline that the sampled hadronic EoSs based on the HS statistic model which do not contain hyperons (HS (TMA), HS (TM1), HS (NL3), SFHO and SFHX) seem to lose convexity in a narrow range of baryonic number densities with a typical width $\Delta n \sim 0.02 \text{ fm}^{-3}$. The large variations of $\mathcal{G}_{(C)}$ and $\mathcal{G}_{(R)}$ in the inhomogeneous to homogeneous nuclear matter transition found in the previous EoSs are associated to remarkably non smooth behavior of the sound speed, which sinks significantly ($c_{s(R)} \lesssim 5 \times 10^{-3} c$) in the range $0.06 \text{ fm}^{-3} \lesssim n \lesssim 0.09 \text{ fm}^{-3}$, precisely, in the mixed phase (as we have indicated above). The PT from non-uniform to uniform nuclear matter is treated with the same Maxwell construction as in the case of the LS220 EoS according to Hempel & Schaffner-Bielich (2010). We observe, however, that the fundamental derivatives become negative in all three variants of the HS EoS independently of the entropy per baryon (Figs. 2 and 3; bottom panels).

The different variants of the GSHen EoS display neither a negative fundamental derivative nor very large oscillations in the region of transition from nuclei to nuclear matter. Shen et al. (2011a) claim that their construction for the PT accounts for the Coulomb interactions. According to the former authors, Coulomb interactions are non-negligible in large astrophysical systems (in contrast to small systems such as the ones found in heavy-ion collisions) and result in a non-uniform phase (across the PT) where the average proton density equals the electron density. For that non-uniform phase Shen et al. (2011a) obtain a monotonic increase of the adiabatic index, Γ_1 , with the number density, contrasting with the decrease in Γ_1 shown by the LS220. Without entering into a deeper discussion on whether the aforementioned PT is of first-order or of any other kind, for what matters this paper, none of the two EoSs (LS220 and GSHen) shows a loss of convexity in the transit from non-uniform to uniform nuclear matter (unless Λ hyperons are included in the LS220 (Λ) EoS; see below).

2.2.1.2 Hyperon phase transition. We note that the appearance of hyperons in the BHB ($\Lambda\phi$) EoS generates a non-convex thermodynamics if the entropy per baryon is large enough at baryonic number densities $n \sim 0.15 \text{ fm}^{-3}$ (Fig. 3). Banik et al. (2014) claim that they “did not find any indication for a first-order phase transition in connection to the appearance of Λ hyperons”. This conclusion is extracted on the basis of the smoothness of the pressure growth with baryon density even after the appearance of Λ hyper-

ons. However, a close look to their Fig. 9 reveals that the entropy is non-smooth precisely where hyperons appear (in their case at baryon densities $\lesssim 10^{15} \text{ gr cm}^{-3}$). This behaviour is reflected in the non-smoothness of the sound speed in two different number density intervals, of which, the one happening at higher entropy per baryon ($s = 2.5$) and $n \simeq 0.15 \text{ fm}^{-3}$ yields negative values of the fundamental derivatives. This is a first evidence of thermodynamic convexity loss connected to the hyperonic phase.

The incorporation of hyperons in the LS220 (Λ) EoS brings a loss of convexity at entropies per baryon $s = 2.5$ (Fig. 3) in the transition from inhomogeneous to homogeneous nuclear matter (note also the behaviour of the sound speed at number densities $0.4 \text{ fm}^{-3} \lesssim n \lesssim 0.6 \text{ fm}^{-3}$ in Fig. 1 for $s = 2.5$). For values $s = 3.5$ this convexity loss is not found (because this larger entropy is also associated to larger temperatures at which the transition to homogeneous nuclear matter disappears), and thus the results at low values of s are linked to the Maxwell construction across a first-order PT (see the discussion in Sect. 2.2.1). We note that the variant of the LS220 EoS that does not incorporate hyperons (LS220) shows positive fundamental derivatives there.

In contrast to the BHB ($\Lambda\phi$) and LS220 (Λ) EoSs, convexity is not lost in the case of the CMF model implemented in the CMF (Λ) EoS, which also incorporates hyperons. In the CMF (Λ), the nuclear PT takes place as a smooth crossover due to the requirements of beta equilibrium and charge neutrality (c.f. Dexheimer & Schramm 2008), at least that the entropies per baryon we consider here, and consistently, the numerical fundamental derivatives remain positive and smooth as can be seen in Figs. 2 and 3.

The HS (DDY2) EoS also incorporates hyperons using the same recipe for its incorporation as in the BHB ($\Lambda\phi$) EoS and, thus, one may observe the same behaviour for the former EoS as for the latter in terms of loss of convexity.

2.2.1.3 Quarks phase transition. Our knowledge of the QCD phase diagram suggests the existence of a QGP PT within the range of densities and temperatures on reach of core collapse events (c.f. Oertel et al. 2012, see also Haensel et al. 2007). The incorporation of a quark phase in the STOS (B165) EoS displays a noticeable impact on the fundamental derivatives, which, however, never become negative in spite of the fact that the hadron-quark transition is of first-order type in this EoS (note the difference in the slopes of the Gibbs free energy in the hadronic and quark phases observed in Nakazato et al. (2008); Fig. 3, the right panels). We should bear in mind that both the STOS and STOS (B165) are more coarsely tabulated than most of the other EoSs considered here. Hence, we shall conclude that the fact that we do not observe negative values of $\mathcal{G}_{(C)}$ in the latter EoS is the result of an insufficiently fine tabulation close to the thermodynamical boundaries of the PT to quark matter. This conclusion is reinforced by the comparison of the EoS CMF (Λ) and CMF (ΛB), which only differ in the incorporation of a first-order NCPT to quarks in the latter. As we can see in Figs. 2 and 3, for $n \gtrsim 0.6 \text{ fm}^{-3}$, there is a rather broad region where $\mathcal{G}_{(C)} < 0$, corresponding to the pronounced drop of the sound speed at such number densities (Fig. 1).

2.2.2 Genuinely relativistic convexity loss

The loss of convexity at $n \gtrsim 0.8 \text{ fm}^{-3}$ and low entropy per baryon is a very robust finding in the case of GSHen (NL3) (Fig. 2; blue line in the upper row). This is, indeed, a genuinely relativistic effect since it happens due to the large value of the sound speed ($0.8 < c_{s(R)}/c < 1$; Fig. 1) and the corresponding action of the term

$-3c_{s(R)}^2/2$ ” in Eq. (2). We note that, differently from the case of the LS220 EoS (see Sec.2.2.3), this happens in a fully causal region for the GSHen (NL3). Remarkably, the same convexity-loss is observed for the HS (NL3) EoS (Fig. 2; blue line in the bottom row), which shares with the GSHen (NL3) EoS the same RMF parameterization (NL3). Nevertheless, in the case of HS (NL3) the relativistic fundamental derivative is also negative at larger entropies per baryon (Fig. 3; blue line in the bottom row). Using the GSHen (NL3) table available at the CompOSE database, it was not possible to obtain thermodynamic values along the $s = 2.5$ isentrope for $n \gtrsim 0.55 \text{ fm}^{-3}$ in the case of GSHen (NL3). In contrast, for the HS (NL3) table, one may compute values along the same isentrope up to $n \lesssim 4.79 \text{ fm}^{-3}$. This happens because of the different tabular limits of both EoSs. While the GSHen (NL3) table provides nodal points in the ranges $10^{-8} \text{ fm}^{-3} \leq n \lesssim 1.5 \text{ fm}^{-3}$ and $0.16 \text{ MeV} \lesssim T \lesssim 75 \text{ MeV}$, the HS (NL3) table extends further the previous ranges to $10^{-12} \text{ fm}^{-3} \leq n \lesssim 10 \text{ fm}^{-3}$ and $0.1 \text{ MeV} \lesssim T \lesssim 158 \text{ MeV}$. Particularly, the larger values of T tabulated in the HS (NL3) EoS allow prolonging the $s = 2.5$ isentrope to larger number densities per baryon. In spite of this technical limitation, and regarding that at high densities and entropies, i.e. for homogeneous matter, both EoS should provide the same results (since the underlying models -NL3- are the same), we also conclude that also the GSHen (NL3) EoS is (relativistically) non-convex at high number-density and entropy per baryon.

2.2.3 Non-physical loss of convexity

None of the two variants of the Lattimer & Swesty (1991) EoS are causal at high enough densities. This has the implication that the sound speed predicted by these EoSs is larger than the speed of light (see the region with $n \gtrsim 1.3 \text{ fm}^{-3}$ in Fig. 1). Consistently, the relativistic fundamental derivative becomes negative (see Figs. 2 and 3 at baryonic number densities $n \gtrsim 1.3 \text{ fm}^{-3}$). This happens because of the action of the term $-3c_{s(R)}^2/2$ in Eq. (2), which becomes a dominant (negative) contribution as the sound speed approaches (and eventually overtakes) the speed of light (see, e.g. Ibáñez et al. 2013). The loss of convexity displayed by both LS220 EoSs in non-causal (high-density) thermodynamic regions, is non-physical.

The large amplitude oscillations observed for the GSHen (FSU1) EoS at high number densities are likely numerical artifacts (see App. A).

3 A PHENOMENOLOGICAL NON-CONVEX EOS

The traditional (simple) way to mimic the complex thermodynamical processes taking place inside a collapsing stellar core in simulations of hydrodynamical supernovae leading to the formation of compact objects, or during the merger of neutron stars in a compact binary system, is to consider EoSs of polytropic-type. Some examples include (i) a polytropic EoS where ‘gamma’ is a discontinuous function of the density (van Riper 1978), (ii) the piecewise-polytropic approximation (Müller & Eriguchi 1985), and (iii) the hybrid polytropic EoS, in which the pressure is composed of a cold component, p_c , described by a polytrope of adiabatic index Γ_c , and an ideal-gas component which incorporates the thermal effects, p_t (see e.g. Maione et al. 2016). We name the latter EoS ‘PolyTh’ and present a detailed analysis of its properties in Appendix B.

In order to explore the fundamental traits of a relativistic non-convex dynamics induced by a non-convex thermodynamics we use a phenomenological EoS introduced in Ibáñez et al. (2018). Here

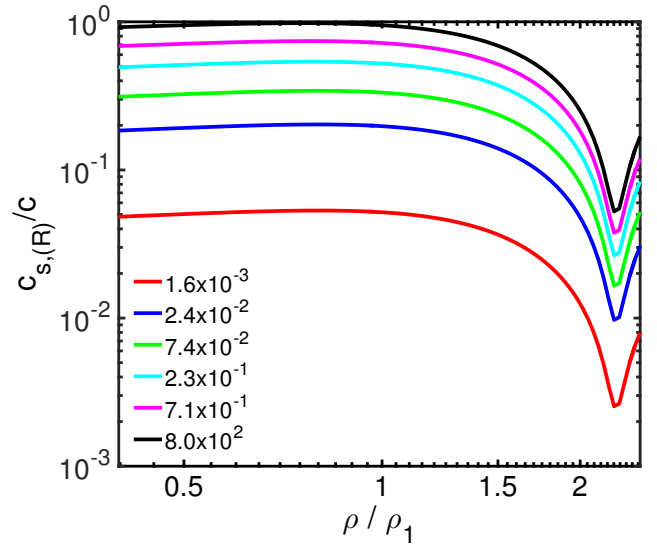


Figure 4. Relativistic speed of sound versus density for the GLL-EoS ($\gamma_0 = 4/3, \gamma_1 = 1.9, \sigma = 1.1, \rho_1 = 10^{15} \text{ g cm}^{-3}$). The curves are parameterized by the specific internal energy, using the particular values indicated in the legend (in units of c^2).

we recap the essentials of the analysis performed on Ibáñez et al. (2018) regarding the non-convex properties that this EoS possess. We begin by the expression of the pressure p , which obeys an ideal-gas-like EoS of the form

$$p = (\gamma - 1)\rho\varepsilon, \quad (7)$$

where γ depends on the density according to the following law:

$$\gamma := \gamma_0 + \mathcal{K} \exp\left(-\frac{x^2}{\sigma^2}\right), \quad \mathcal{K} := \gamma_1 - \gamma_0, \quad x := \rho - \rho_1, \quad (8)$$

and where ε and ρ are, respectively, the specific internal energy and the rest-mass density. We note that in Ibáñez et al. (2018) the pressure contains an additive term of the form $B\rho$, which depends on another free parameter of the EoS. Hereafter, we restrict to the case $B = 0$. Ibáñez et al. (2018) proposal for γ in Eq. (8) can be considered as a generalization of the classical prescription used in early studies of core-collapse supernovae (see e.g. van Riper 1978). The function $\gamma(\rho)$ in Eq. (8) reaches a maximum at $\rho = \rho_1$, a value we designate as $\gamma_1 = \gamma(\rho_1)$. Let us notice that ρ_1 plays the role of a simple scale factor for the density, if we express the *width* of the Gaussian law (σ) in units of ρ_1 too, convention we adopt in the following. The EoS defined by Eqs. (7) and (8) will be named hereafter ‘GGL-EoS’ (for Gaussian Gamma Law). The reference parameters we chose to analyse its properties are $\gamma_0 = 4/3, \gamma_1 = 1.9, \sigma = 1.1$, and $\rho_1 = 10^{15} \text{ g cm}^{-3}$. The values of γ_0 and γ_1 mimic the behaviour of collapsing dense matter during the standard prompt mechanism of hydrodynamical supernovae, before and after core bounce (see, e.g. Janka et al. 2012).

Applying the definition of the classical speed of sound (Eq. 3) to our GGL-EoS, we obtain

$$c_{s(c)}^2 = \gamma \left(\frac{p}{\rho} + \varepsilon \frac{d \ln \gamma}{d \ln \rho} \right) = \gamma \varepsilon \left(\gamma - 1 + \frac{d \ln \gamma}{d \ln \rho} \right). \quad (9)$$

For later reference, we also write the specific enthalpy for the GGL-EoS:

$$h = 1 + \gamma\varepsilon. \quad (10)$$

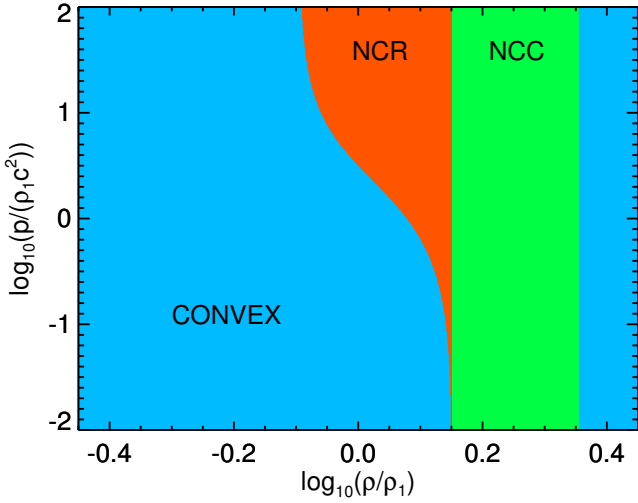


Figure 5. Regions of the $P-\rho$ plane of the GLL-EoS with parameters $\gamma_0 = 4/3$, $\gamma_1 = 1.9$, $\sigma = 1.1$, and $\rho_1 = 10^{15} \text{ g cm}^{-3}$, displayed in different colors according to their convexity (lack thereof) properties. The blue colored area corresponds the region of the parameter space where both $\mathcal{G}_{(C)} > 0$ and $\mathcal{G}_{(R)} > 0$, i.e., where the EoS exhibits a convex-thermodynamics. The red colored area corresponds to the region of the parameter space where $\mathcal{G}_{(C)} > 0$ and $\mathcal{G}_{(R)} \leq 0$, i.e., the EoS is non-convex from the relativistic point of view (NCR). Finally, the green colored area corresponds to the region of classical non-convexity (NCC), in which $\mathcal{G}_{(C)} \leq 0$ and $\mathcal{G}_{(R)} \leq 0$.

Figure 4 shows, in logarithmic scale, the relativistic speed of sound (in units of the speed of light c) as a function of the density, parameterized by the specific internal energy. We note that the parameterization used in the GLL-EoS avoids non-causality (i.e., yields $c_{s(R)} < c$) and leads to very low values of $c_{s(R)}$ for densities much higher than ρ_1 . As the legend of Fig. 4 indicates, $c_{s(R)}$ is an increasing function of ε .

The explicit expressions for the adiabatic index, Γ_1 (see e.g. Chandrasekhar 1939), and the fundamental derivatives for the GLL-EoS have been obtained in Ibáñez et al. (2018). The adiabatic index (Eq. 4), which is in general $\Gamma_1 \neq \gamma$, reads

$$\Gamma_1 = \gamma \left\{ 1 + \left(\frac{\rho \varepsilon}{p} \right) \frac{d \ln \gamma}{d \ln \rho} \right\}. \quad (11)$$

The classical fundamental derivative for our GLL-EoS is:

$$\mathcal{G}_{(C)} = \mathcal{G}^+ + \frac{\gamma \varepsilon}{2c_{s(C)}^2} \left(\gamma \frac{d \ln \gamma}{d \ln \rho} + \frac{d^2 \ln \gamma}{d (\ln \rho)^2} \right), \quad (12)$$

where

$$\mathcal{G}^+ := \frac{1}{2} \left\{ 1 + \gamma + \left(\frac{d \ln \gamma}{d \ln \rho} \right) \right\}. \quad (13)$$

From the above equation and the expression for $c_{s(C)}^2$ given by Eq. (9) it is easy to conclude that $\mathcal{G}_{(C)}$ is independent of ε .

Figure 5 shows the regions of the $P-\rho$ plane in which the GLL-EoS is divided in terms of the character of the thermodynamics. We observe that with the exception of a small region around and above ρ_1 , the EoS is convex, i.e., the classical and relativistic fundamental derivatives, satisfy $\mathcal{G}_{(R)} > 0$ and $\mathcal{G}_{(C)} > 0$ (blue region in Fig. 5). In the green region $\mathcal{G}_{(C)} \leq 0$, and, as a result, so is $\mathcal{G}_{(R)} \leq 0$. This is a non-convex classical (NCC) region of the EoS. There is also a non-convex relativistic (NCR) region in which only $\mathcal{G}_{(R)} < 0$, while $\mathcal{G}_{(C)} > 0$ (red region in Fig. 5).

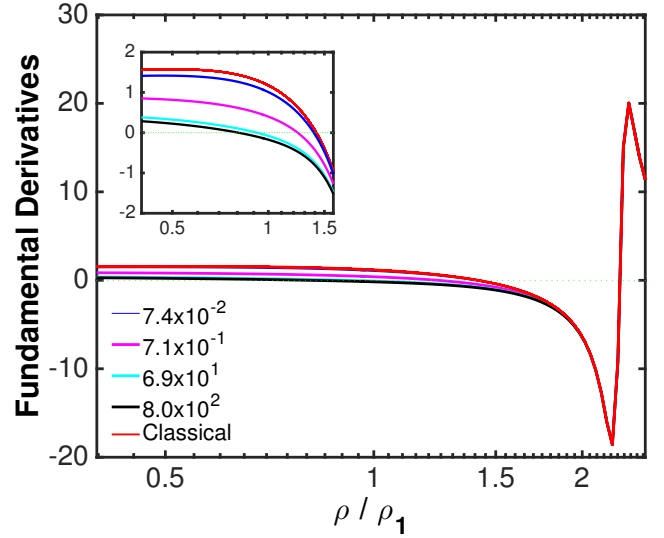


Figure 6. Classical and relativistic fundamental derivatives as a function of density for the GLL-EoS. The classical fundamental derivative is indicated by a red thick line. The relativistic fundamental derivative is parameterized by the specific internal energy, with the particular values indicated in the legend. The inset shows a detail of the region around $\rho = \rho_1$.

Figure 6 shows the two fundamental derivatives, classical (red thick line) and relativistic, as a function of density, being $\mathcal{G}_{(R)}$ parameterized by the specific internal energy. The inset shows a detail of the region around $\rho = \rho_1$ in order to highlight that, according to Eq. (2), $\mathcal{G}_{(C)}$ is an upper bound of $\mathcal{G}_{(R)}$. Furthermore, the inset clearly displays the existence of regions for which $\mathcal{G}_{(R)} \leq 0$ and $\mathcal{G}_{(C)} \geq 0$ simultaneously. We point out the qualitative similarity between the behaviour of the fundamental derivatives of the GLL-EoS around $\rho = \rho_1$ compared with that of a number of microphysical EoSs at high enough number density (see Figs. 2 and 3). Note that, in the case of the GLL-EoS, the convexity-loss around $\rho = \rho_1$ is not related to any PT, which does not exist in the phenomenological EoS. This point is relevant inasmuch as the convexity loss of several microphysical EoSs at baryon densities around the PT to uniform nuclear matter may result from the explicit construction employed to deal with the mixed phase in a thermodynamically consistent way.

4 EQUILIBRIUM CONFIGURATIONS

We turn next to analyze spherically-symmetric configurations of relativistic stars in equilibrium that satisfy the GLL-EoS introduced in the previous section. The relationship between the specific internal energy and the rest-mass density follows from the first law of thermodynamics for adiabatic processes. The corresponding ordinary differential equation, for our GLL-EoS, can be written as

$$\frac{d \ln \varepsilon}{d \ln \rho} = \gamma(\rho) - 1. \quad (14)$$

The integration constant in the above equation can be defined from the polytropic form ($p = \kappa_{\text{dnr}} \rho^{\Gamma_{\text{dnr}}}$) of the EoS for a degenerate ideal Fermi gas of electrons at very low densities, i.e. the degenerate non-relativistic regime (dnr), where $\kappa_{\text{dnr}} = 1.0036 \times 10^{13} Y_e^{5/3}$ (in CGS units, and $Y_e = 1/2$). In practice, and in order to obtain values of the maximum gravitational mass (see below) compatible with

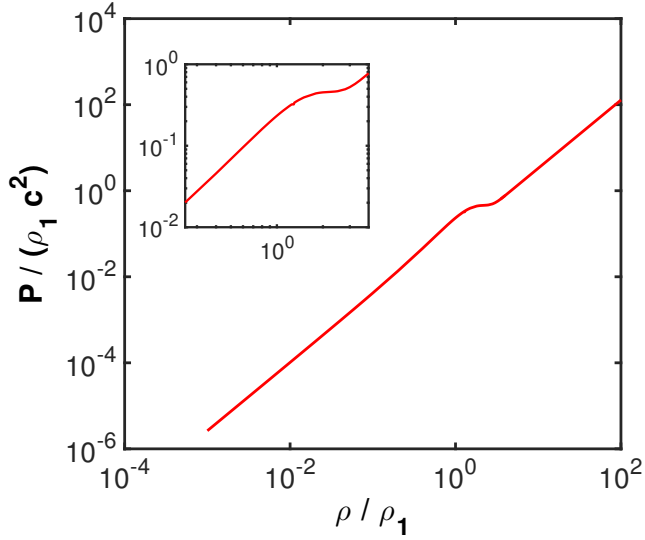


Figure 7. GGL-EoS: pressure versus density, parameterized by the specific internal energy given by the fit shown in Eq. (15). The inset shows a detail around the value ρ_1 .

current observational data, we have verified that an optimal value is $\kappa_{\text{dr}} = 2.0072 \times 10^{12} Y_e^{5/3}$ (i.e. a reduction factor of 1/5).

The resulting tabulated relationship between the specific internal energy and the rest-mass density is fitted with a potential law

$$\varepsilon = \kappa_{\text{ad}} \rho^b, \quad (15)$$

where ε is given in units of c^2 . The fitting parameters are $\kappa_{\text{ad}} = 4.2266 \times 10^{-10}$ and $b = 0.58584$ for a fitting interval $\rho \in [\rho_1^{-1}, 10\rho_1]$. Equations (7), (8) and (15) define completely our GGL-EoS. Figure 7 shows the GGL-EoS used to construct the static equilibrium models in this section and employed in the dynamical evolutions of rotational collapse of neutron stars to BHs in the next one.

In order to obtain spherically-symmetric relativistic equilibrium configurations that obey the GGL-EoS we solve the Tolman-Oppenheimer-Volkoff (TOV) equation. The gravitational mass M_G of the equilibrium configurations, parameterized by the central density ρ_c , is shown in Fig. 8 as a function of the radius. It reaches a maximum $M_G^{\text{max}} = 2.536 M_\odot$, at a central density $\rho_c^{\text{crit}} \approx 1$ (units of ρ_1), being the corresponding radius $R \approx 16.6$ km. The inset displays M_G versus the central density. Models with central densities in the interval $\rho_c^{\text{crit}} \leq \rho_c/\rho_1 \lesssim 1.4$, define a small plateau in the $M_G(\rho_c)$ curve where this function is strictly decreasing, i.e. there is no local maximum. By construction, the models are isentropic and therefore they satisfy the well-known static stability criterion against radial oscillations (Bardeen et al. 1966): the stability region is the one at central densities below the critical one, ρ_c^{crit} , at which the gravitational mass has an absolute maximum. Also shown in Fig. 8 is the region bounded by the Schwarzschild radius (black dots in the upper-left corner of the figure).

Moreover, the specific internal energy and the specific enthalpy are, by definition, increasing functions of the density. Therefore, their maxima (in radius) are reached at the centre of the configuration. For the critical model, the central values of ε and h are, respectively, $\varepsilon = 0.26$ and $h = 1.49$. Thus, the critical model is, from a thermodynamical point of view, only moderately relativistic.

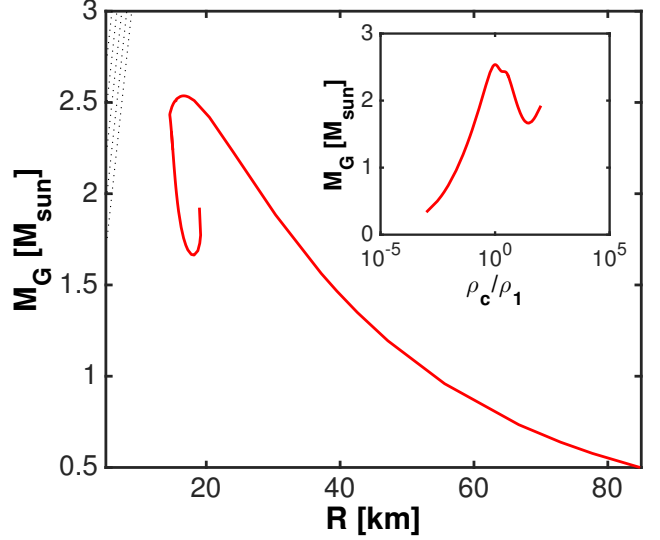


Figure 8. Gravitational mass versus radius of the equilibrium configurations for our GGL-EoS, parameterized by the central density. The black dotted region in the upper-left corner corresponds to $R \leq 2M_G$. The inset shows the gravitational mass versus the central density.

Consistent with our GGL-EoS, the relativistic speed of sound at the centre of the equilibrium configurations is not a monotonic function of the central density. Its central value for the critical model is $c_{s(R)} = 0.546$. This value is an upper bound for all the equilibrium models. Let $\mathcal{C} := \max(2Gm/(rc^2))$ be the maximum value of the compactness parameter, in radius, for each model. For our GGL-EoS the models reach an absolute maximum of $\mathcal{C} = 0.59$ at $\rho_c = 2\rho_1$, being its value at the critical central density $\mathcal{C} = 0.53$.

Figure 9 shows the two fundamental derivatives, $\mathcal{G}_{(R)}$ and $\mathcal{G}_{(C)}$, as a function of the radius, for an equilibrium model obeying the GGL-EoS and with central density $\rho_c/\rho_1 = 1.4$. Due to the particular form of our GGL-EoS, equilibrium models with central densities larger than the critical one will develop non-convex thermodynamics. For the sequence of equilibrium models we compute, there exists a small interval of central densities, namely $1.3 \lesssim \rho_c/\rho_1 \lesssim 1.4$, in which $\mathcal{G}_{(R)} < 0$ and $\mathcal{G}_{(C)} > 0$. This is shown in Fig. 9 for the particular case $\rho_c/\rho_1 = 1.4$. As a result, in such a narrow region of central-density values, the innermost cores of our models can develop non-convex thermodynamics induced by purely relativistic effects. The dynamical collapse of these objects, if perturbed, would rapidly trigger the presence of compound waves induced by such non-convex thermodynamics. Alternatively, the presence of non-convex relativistic regions may also induce a non-standard dynamics as a result of the non-monotonic dependence of the sound speed with the rest-mass density. We investigate the aforementioned possibilities in the next sections.

5 GRAVITATIONAL COLLAPSE IN SPHERICAL SYMMETRY

Within the framework of the GGL-EoS, the most promising scenario for encountering non-convex effects is the collapse of a star with a central density, ρ_c , similar to or above of ρ_1 . We explore this possibility first in spherically symmetric simulations of toy models for neutron stars, comparing two equations of state. Four models were simulated with the GGL-EoS with different parameters and

model name	IC	γ_1	ρ_1 $10^{15} \text{ gr cm}^{-3}$	EoS	ρ_c $10^{15} \text{ gr cm}^{-3}$	M_0 M_\odot	R_0 [km]	ξ	t_{BH} [ms]
P-1.9G	P	1.9	1.0	GGL	2.18	1.39	10.0	1.39	0.066
P-1.9S	P	1.9	1.0	SGGL	2.18	1.39	10.0	1.39	0.186
P-1.6G	P	1.6	1.0	GGL	2.18	1.39	10.0	1.39	0.063
P-1.45G	P	1.45	1.0	GGL	2.18	1.39	10.0	1.39	0.063
G-1.9G	G	1.9	1.0	GGL	2.18	1.28	10.6	1.21	0.117
S-1.9S	S	1.9	1.00	SGGL	2.18	1.33	11.3	1.18	0.166
P-1.9G1	P	1.9	0.9356	GGL	2.046	1.98	11.8	1.68	0.068
P-1.9G2	P	1.9	1.00	GGL	2.046	1.98	11.8	1.68	0.073
P-1.9G3	P	1.9	1.31	GGL	2.046	1.98	11.8	1.68	0.093
P-1.9G4	P	1.9	1.559	GGL	2.046	1.98	11.8	1.68	0.111

Table 1. List of spherically symmetric, non-rotating models. For each model (name in the first column), the second column states the initial conditions (P, G, and S standing for the polytropic model and the ones computed with the GGL-EoS and SGGL-EoS, respectively). The further columns characterize the EoS used in the simulation: the parameters γ_1 and ρ_1 are given in the third column and fourth columns, while in the fifth column we list that the variant of the GGL-EoS employed in the run. Finally, in the last four columns, we provide the mass, the radius and the compactness of the initial configuration, as well as the time of formation of the BH, respectively.

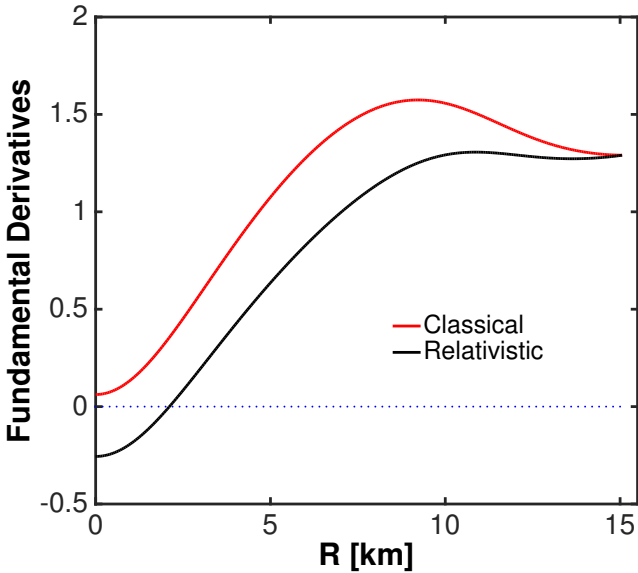


Figure 9. Radial profiles of the classical (red curve) and relativistic (black curve) fundamental derivatives for an equilibrium model with $\rho_c/\rho_1 = 1.4$ and obeying the GGL-EoS.

two with a modified version thereof, which we call Semi-GGL-EoS (SGGL-EoS). It consists of the GGL-EoS, but with a flat rather than decaying adiabatic index above ρ_1 :

$$\begin{aligned} \gamma^{\text{SGGL}} &= \gamma^{\text{GGL}}(\min(\rho, \rho_1)) \\ &= \gamma_0 + \mathcal{K} \exp\left(-\frac{\min(\rho, \rho_1) - \rho_1}{\sigma^2}\right). \end{aligned} \quad (16)$$

This EoS maintains the stiffening of the GGL-EoS at $\rho = \rho_1$, but its avoidance of the non-convexity at high densities allows us to gauge the importance of non-convex dynamics.

We consider three different initial models, all of which have been constructed by solving the TOV equation, albeit using different EoSs:

(i) The first one is a star with a polytropic EoS, $p = \kappa \rho^\gamma$, with a single adiabatic index $\gamma = 2$ for all densities and $\kappa = 8.422 \times 10^4$ in CGS units.

(ii) The second model was computed with the GGL-EoS, fol-

lowing the prescription developed in Sec. 4, but with the following parameters: $\gamma_0 = 4/3$, $\gamma_1 = 1.9$, $\sigma = 1.1$, $\rho_1 = 10^{15} \text{ g cm}^{-3}$.

(iii) In the third type of model, we use the SGGL-EoS (again following the prescription developed in Sec. 4) with the same parameters as in the point (ii).

For numerical reasons, we endow our initial configurations with a power-law decaying atmosphere for values of the rest-mass density $\rho \lesssim 10^{-10} \rho_c$, where ρ_c is the central rest-mass density. This atmosphere possesses a dynamically negligible mass. Irrespective of the type of initial model, we simulate the models with the GGL-EoS or SGGL-EoS.

All initial models have the central rest-mass density in the range $\rho_c \approx 2.05 \times 10^{15} - 2.18 \times 10^{15} \text{ g cm}^{-3}$, which is about twice the parameter ρ_1 . The mass of the initial configurations are either $M_0 \approx 1.39 M_\odot$ or $M_0 \approx 1.98 M_\odot$ (see Table 1). These two masses roughly bracket the mass of the iron cores of massive stars (from which collapse a neutron star remnant may result) with main sequence masses in the range $10 M_\odot - 120 M_\odot$ and solar metallicity (Woosley & Heger 2007). They are initially in equilibrium, but an *ad hoc* reduction of the pressure will trigger their collapse. Indeed, the reason to choose three different EoS to construct the initial model is that we aim to assess the dynamical effects of the *ad hoc* initialization of the collapse on the subsequent dynamics. In the polytropic initial models, the reduction of the pressure is the result of the switch to the (S)GGL-EoS, while in the initial models with GGL-EoS it is brought about by a uniform reduction of the internal energy density by 15%. Following O'Connor & Ott (2011), we define a compactness parameter as

$$\xi := \frac{M_0/M_\odot}{R_0/10 \text{ km}}, \quad (17)$$

where M_0 and R_0 are the initial mass and radius, respectively, of the equilibrium configuration.⁶ According to this definition, the initial models built with a polytropic EoS are more compact than models constructed with the (S)GGL-EoS. The models having larger mass ($M_0 = 1.98 M_\odot$; Table 1) feature the largest compactness. Consistent with the large compactness of our models, we do not expect them to develop supernova explosions, even if a detailed neutrino physics and energy transport or magnetic fields were included in our simulations. Certainly, both of these effects may slightly

⁶ Note the difference in the definition of *compactness*, \mathcal{C} , used in Sec. 4.

change the dynamics, but for the purpose of assessing exclusively the impact on the dynamics of the convexity loss, we may neglect them.

The simulations were performed with a version of the code AENUS employed in Obergaulinger & Aloy (2017) and Obergaulinger et al. (2018), but restricted to special relativistic hydrodynamics, using fifth-order monotonicity preserving reconstruction schemes and an HLL Riemann solver. Gravity was incorporated using the pseudo-relativistic TOV potential of Marek et al. (2006), which provides a very good approximation to full GR in spherical symmetry. Once the center collapses to a BH, we excise the innermost region. The excision is undertaken by following the evolution of the lapse function, α related to the pseudo-relativistic TOV potential, Φ , by $\alpha \simeq \exp(\Phi/c^2)$. Numerical cells that develop $\alpha \leq \alpha_{\text{th}} := 0.018$ in the course of the evolution are *frozen*, except for a gauge transformation, which shifts their position from their location when they hit the condition $\alpha = \alpha_{\text{th}}$, $r = r_{\text{AH}}$ (where r_{AH} is the radius of the apparent horizon) to $r = 0$ by means of a suitable radial shift, β_r , on a time scale r_{AH}/β_r . The latter shift greatly diminishes spurious reflections at the apparent horizon location. The simulation grid consists of 3200 zones logarithmically spaced up to an outer radius of 180 km. The large extent of the grid, much larger than the radius of the initial equilibrium configuration, reduces any potential contamination by boundary effects. The minimum grid resolution is $(\Delta r)_{\text{min}} = 100 \text{ m}$.

We present an overview of the time evolution of the six models holding the smaller total mass in the spacetime diagrams shown in Fig. 10. All models collapse quickly, as we see in the high negative velocities (brown shades in Fig. 10) and the contracting iso-density contours. Black holes are formed promptly, between 0.06 and 0.19 ms as can be seen from the growth of the white regions for $r < 3 \text{ km}$ in the aforementioned figure and from the last column of Table 1. This time scale can be compared with the light-crossing time of the initial configurations, which range between 0.033 and 0.038 ms. We note that the surface of the neutron star, visible as a large concentration of iso-density (dark-green) contours initially at about 10 km Fig. 10, falls towards the center. In models with the standard GGL-EoS, the whole neutron star is accreted, whereas it avoids this fate for the model initially built and later evolved with the SGGL-EoS, where a shock wave is launched at the surface and ejects parts of the matter (blue shades in the lower right panel of Fig. 10). This effect is, however, only circumstantial to our analysis since it is not connected to the appearance of non-convex regions in the star. It is an artefact due to the artificial atmosphere that surrounds the initial configuration, which is necessary for numerical reasons. Instead, we turn our attention to the central regions before the formation of the BH.

Model P-1.9G (top left panel of Fig. 10) possesses regions where the EoS is non-convex right from the beginning: all gas inside radii of $r_{\text{ncr}} \approx 4.8 \text{ km}$ and $r_{\text{ncc}} \approx 4.0 \text{ km}$ is relativistically and classically non-convex (cf. the orange and red lines). As the collapse accelerates, velocities become supersonic and sonic points form at $t \approx 0.01 \text{ ms}$ and $r_{\text{sp}} \approx 2.1 \text{ km}$ (white lines). Note that differently from a standard collapse developed with a fully convex EoS (of which model P-1.9S is an example), two separated sonic points form relatively close to the stellar center (i.e. detached from the -artificial- dynamics of the nearly free-falling stellar surface). This is because of the non-monotonicity of the sound speed dependence with density (e.g. Fig. 4). Shortly afterwards, the density increases sufficiently for the central regions to become convex. At $t \approx 0.03 \text{ ms}$, the inner sonic point and the boundary between convex and non-convex regions merge. At this point, a shock wave forms at

this transition (in the spacetime diagram, it appears as a transition from darker to lighter brown in the radial velocity maps starting at $r \sim 2.8 \text{ km}$, and following the innermost white line). We highlight the fact that the formed shock is compressive and not expansive, as one would guess from the fact that it is produced in a non-convex thermodynamic region. Differentiating between a compressive and an expansive shock is not straightforward with an Eulerian numerical method, since the Rankine-Hugoniot jump conditions do not exactly hold in the discrete numerical solution. The shock is moving inwards for an observer at rest with respect to the center of the star (see upper panels of Fig. 12). Thus one could draw the (erroneous) conclusion that the state *upstream* of the shock is that located to its left, while the state *downstream* of the shock is located to its right. If this were the case, subsonic matter in the region upstream of the shock would cross it and end up in a supersonic region. That would be interpreted as a sign of an expansion shock. This conclusion is erroneous because matter is collapsing (almost free-falling). Observing the lower panels of Fig. 12, the shock clearly progresses increasing the mass enclosed (to the left of the shock). Thus, the lower panels unambiguously show that the state upstream of the shock is located towards larger mass-coordinate (i.e. to the right of the shock). This state is supersonic and matter crosses the *compression* shock and accumulates in the downstream subsonic part of the flow. Since the compactness of our cores is so large, the collapse is too violent for the shock wave to propagate outwards or explode the star. Instead, it remains an accretion shock through which gas falls towards the center. Furthermore, it is rather short-lived and disappears at $t \approx 0.065 \text{ ms}$ inside the nascent BH. After BH formation at $t \approx 0.066 \text{ ms}$ the sonic point initially located closer to the center falls on the growing apparent horizon, which becomes a transonic point thereafter. The second sonic point, initially located further off center, soon follows the same fate and touches the apparent horizon at $t \approx 0.013 \text{ ms}$. Meanwhile, the collapsing outer stellar shells speed up and become supersonic, first close to the infalling surface and a bit later closer to the apparent horizon. The formation of another sonic point right at the location where the initial atmosphere is set up (a point that is also free falling with the rest of the star) is an artefact of the atmospheric initialization. After most of the mass falls onto the BH ($t \approx 0.14 \text{ ms}$) this artificial sonic point remains steady at a distance of $r \approx 3.6 \text{ km}$. From there on, the dynamics ceases and a steady accretion of the artificial atmosphere goes on. We stress again that the mass in the atmosphere is totally negligible with respect to the initial mass of the model.

Reducing γ_1 to a value of $\gamma_1 = 1.6$ (model P-1.6G, top right panel of Fig. 10) leads to a faster collapse and reduces the extent of non-convex regions. Although sonic points form as in the previous model, they do not align with the border of the non-convex region. A compression shock forms, but it is much weaker than before, hardly noticeable in the space-time diagram. A further reduction to $\gamma_1 = 1.45$ (model P-1.45G, middle left panel) entirely removes the non-convex region. No shock can be observed, and the collapse proceeds smoothly. This statement does not hold for model P-1.9S (middle right panel), where we use the SGGL-EoS with $\gamma_1 = 1.9$. In this case, the absence of non-convex regions is not due to the low value of γ_1 , but to the constant adiabatic index above ρ_1 . This case demonstrates that the appearance of a (compression) shock wave is not solely connected to the value of γ_1 , but to the non-convexity. This remark is relevant in view of the fact that virtually all EoS of nuclear matter yield values of γ significantly larger than $\gamma_1 = 1.45$ for rest-mass densities above $\sim 10^{14} \text{ gr cm}^{-3}$.

The two models with the initial data constructed for the (S)GGL-EoS (G-1.9G and S-1.9S, bottom panels of Fig. 10) con-

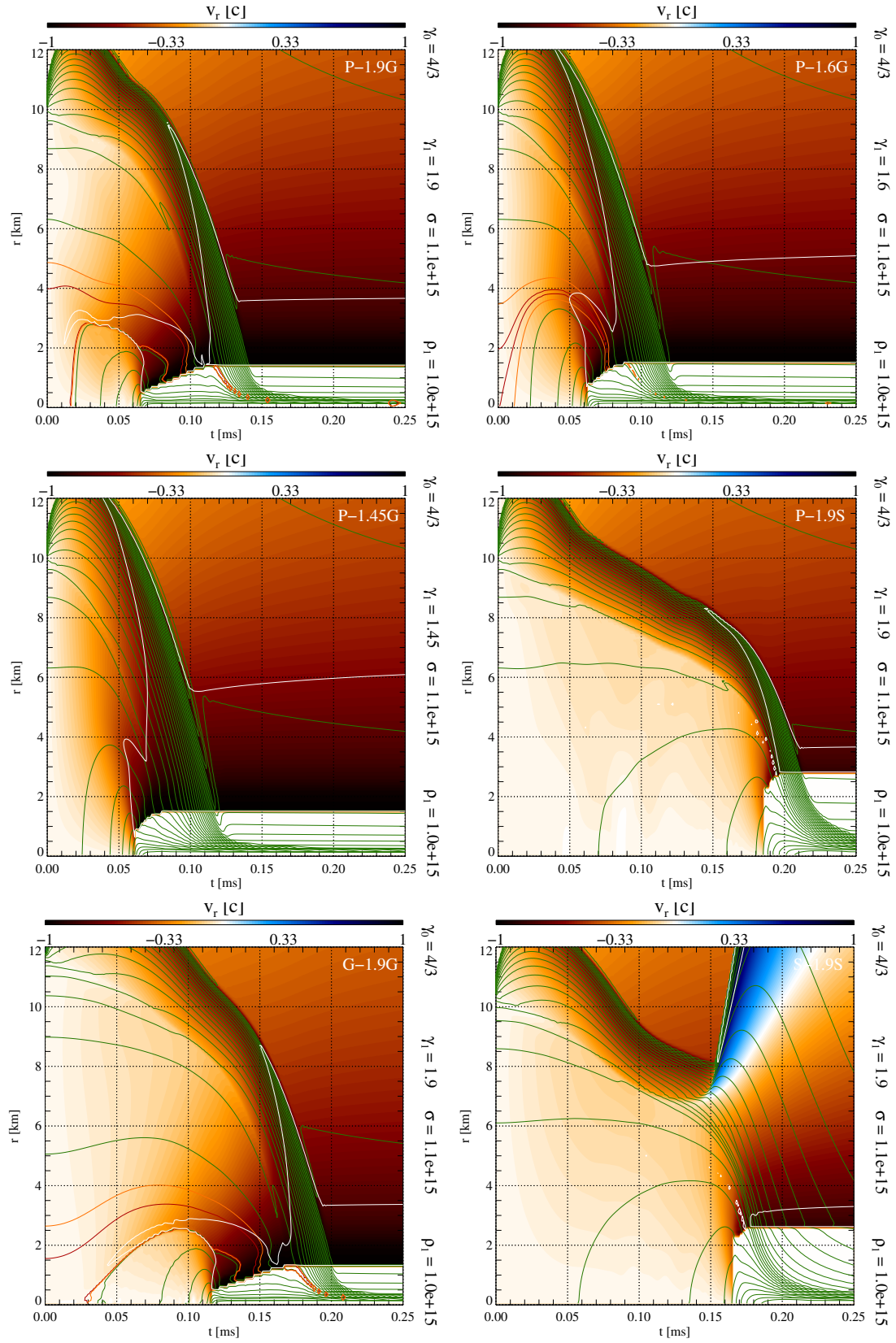


Figure 10. Evolution of six different spherically symmetric models, from top left to bottom right P-1.9G, P-1.6G, P-1.45G, P-1.9S, G-1.9G, and S-1.9S. The diagrams show the velocity in units of the speed of light as a function of time and radius. In addition, contours of density (dark green lines) and the boundaries of the regions of classical and relativistic non-convexity are displayed (classical: dark red, relativistic: orange lines; models with the SGGL-EoS do not exhibit such regions) and the locations of the sonic point are marked by white lines. The white region at the bottom of each panel is the excised BH. The black-blue-white, triangular region displayed in the lower right panel corresponds to parts of the self-gravitating configuration that bounce and acquire positive radial speeds.

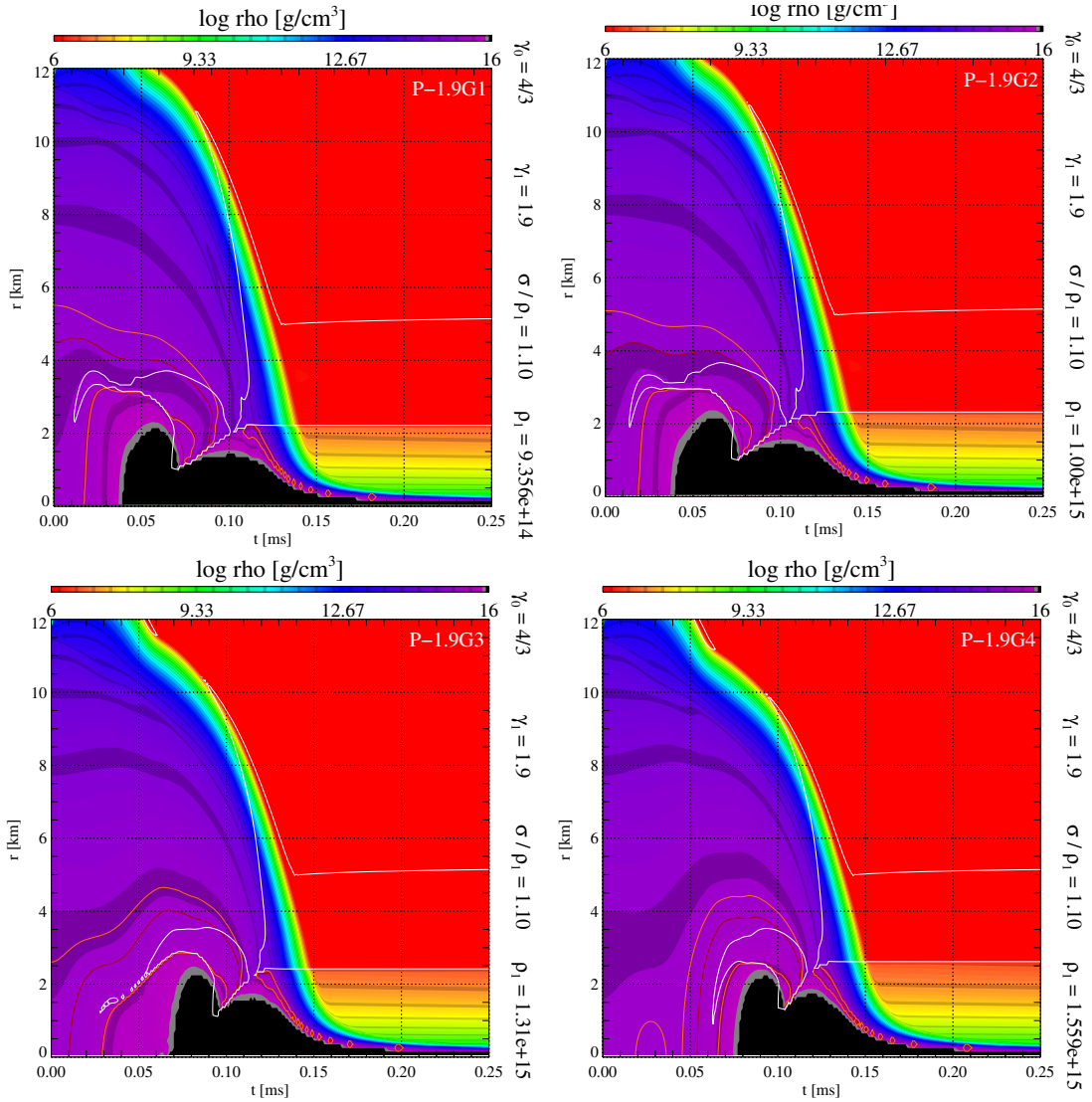


Figure 11. Evolution of four different spherically symmetric models, from top left to bottom right P-1.9G1, P-1.9G2, P-1.9G3 and P-1.9G4. The diagrams show the logarithm of the rest-mass density as a function of time and radius. In addition, the boundaries of the regions of classical and relativistic non-convexity are displayed (classical: dark red, relativistic: orange lines) and the locations of the sonic point are marked by white lines. The black region below the sonic point located at $r \simeq 2.55$ km at the bottom of each panel are excised from the computational domain (it corresponds to the BH).

firm the findings obtained for the polytropic initial models. For the standard GGL-EoS, a compression shock is formed at the inner border of the convex region, where the inner sonic point is situated. Similarly to the polytropic initial model, it does not suffice to explode the star and ultimately ends up in the BH. The model with the SGGL-EoS, on the other hand, does not develop a shock wave in the vicinity of the BH. We stress that the parameters used for both EoS (GGL and SGGL) are the same. Therefore, this result confirms that when convexity is not lost, no shocks form in the course of the collapse to BH. Remarkably, the only difference between, the SGGL EoS and the GGL-EoS is that the former one avoids the convexity loss preventing the steep decline of the adiabatic index after its maximum at $\rho = \rho_1$ (see Eq. (16)). The SGGL-EoS is stiffer than the GGL-EoS at high densities. In spite of this crucial difference, no accretion shock forms using the SGGL-EoS (in contrast to the model run with the GGL-EoS with the same parameters), even if one could argue that a stiffer EoS is more likely prone to produce

bounces in the dynamics with the potential formation of associated shocks.

Models P-1.9G and G-1.9G are evolved with the same GGL-EoS, but differ in the initial configuration, which is polytropic (with $\gamma = 2$) for the former and constructed according to the GGL-EoS with $\gamma_{\max} = \gamma_1 = 1.9$ for the latter. This difference in the initial configuration yields a temporal shift to the overall dynamics, which otherwise is qualitatively the same. We observe a delayed BH formation in model G-1.9G compared to model P-1.9G (see Table 1). Furthermore, the formation of the shock associated with the existence of two sonic points in the collapsing fluid is also present (though delayed) in model G-1.9G. Thus, we conclude that building a polytropic initial model and then evolving it with the GGL-EoS does not introduce major differences either in the qualitative dynamics, nor in the final fate of the collapsing core.

We have also run a series of models having relatively large masses of nearly $2M_{\odot}$. This series is formed by models P-1.9G1, P-1.9G2, P-1.9G3 and P-1.9G4, which have all the same initial poly-

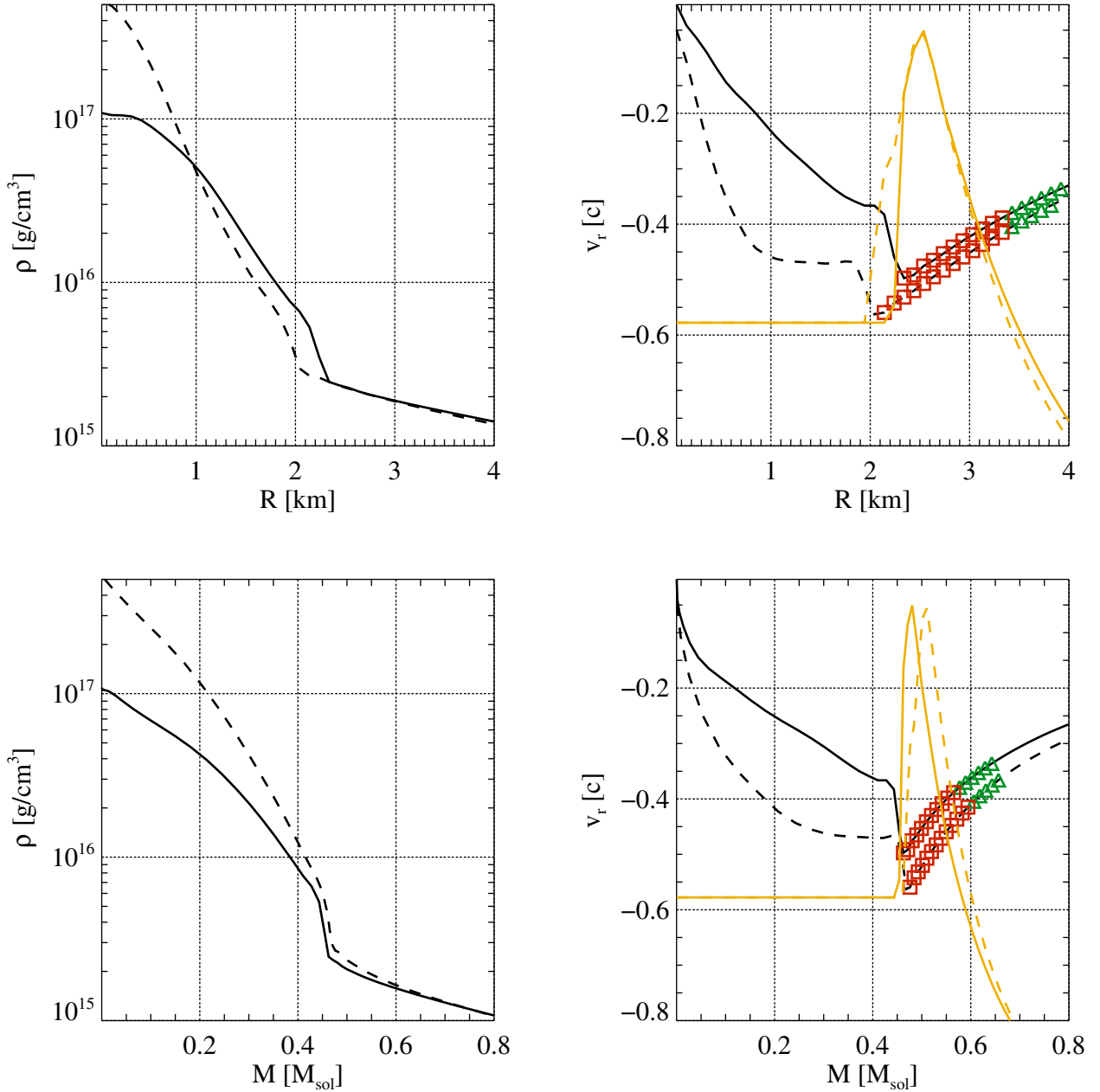


Figure 12. Zoom of selected hydrodynamic properties of model P-1.9G. (Top panels): As a function of the distance to the center of the star we show (left panel) the distribution of the rest-mass density and (right panel) the distribution of the velocity (black lines) and of the sound speed (orange lines). The solid (dashed) lines correspond to a time $t = 0.060$ ms ($t = 0.064$ ms). On the right panel, the non-convex region is marked with symbols: where $\mathcal{G}_{(C)} < 0$ and $\mathcal{G}_{(R)} < 0$ we use red squares, while the region where $\mathcal{G}_{(C)} > 0$ and $\mathcal{G}_{(R)} < 0$ is displayed with green triangles. The accretion shock moves *inwards* from its position $R \simeq 2.3$ km at $t = 0.060$ ms to $R \simeq 2$ km at $t = 0.064$ ms. Note that the shock forms at the boundary between the regions where the classical fundamental derivative changes sign from $\mathcal{G}_{(C)} > 0$ (left to the shock) to $\mathcal{G}_{(C)} < 0$ (right to the shock). Left to the points where $\mathcal{G}_{(C)} = \mathcal{G}_{(R)} = 0$ there is a sonic point in the fluid (another sonic point is located farther away from the center). (Bottom panels): Same as the top panels but as a function of the enclosed mass. The accretion shock moves *outwards* from an enclosed mass $M \simeq 0.45 M_{\odot}$ at $t = 0.060$ ms to $M \simeq 0.46 M_{\odot}$ at $t = 0.064$ ms. Comparing the left and right panels it is easy to see that the sound speed is not a monotonic function of the rest-mass density in the non-convex region.

tropic model ($\gamma = 2$ and $\kappa = 100$ in the same units we employ later in Sec. 6, or, equivalently $\kappa = 3.46 \times 10^5$ in CGS units) but the evolution is followed employing the GGL-EoS with different values of ρ_1 and σ (see Table 1). For the latter, we fix $\sigma = 1.10$ in the former four cases. These models are the non-rotating analogs of the models D1 that we will introduce in the next section (see Tab. 3).

Spacetime diagrams of the logarithm of the rest-mass density of all these models are displayed in Fig. 11. We observe that all of them show the same qualitative behaviour as described for the reference case P-1.9G. From this series of models we observe that BH formation time increases with ρ_1 (see Table 1). In the spacetime evolution of the rest-mass density we observe the much smaller

density of the surrounding (rarefied) atmosphere (red shades in all panels of Fig. 11). We also point out that the BH-excised region displays a density gradient from the values in the atmosphere to the highest densities in the domain (note the regions below the inner sonic point displayed with a white contour, which is nearly horizontal for $t > 0.15$ ms, in all the panels of the figure). This gradient is the result of the radial velocity shift we apply inside of the excised region (see above) to concentrate effectively all the mass in a volume around $r \simeq 0$. There is, however, a small quantitative difference among the P-1.9G1 to P-1.9G4 series of models in the time of shock formation, which is associated with the loss of convexity of the EoS, as in the previous models of lower mass. The region of non-convexity does not appear from the very beginning in model P-1.9G4. There is, first a small region surrounding the center of the star where the relativistic fundamental derivative becomes negative during a brief and transitory episode ($0.02 \text{ ms} \lesssim t \lesssim 0.036 \text{ ms}$). Due to the adjustment of the central region to the loss of convexity, a small oscillation happens and the core slightly expands. Since the collapse is ongoing, the oscillation is very quickly dumped and, once the density in the vicinity of the stellar center grows again above $\simeq \rho_1$, the non-convex region begins to grow from the center (at $t \simeq 0.04 \text{ ms}$) until it reaches a maximum radial extend of $\simeq 4.5 \text{ km}$ at $t \simeq 0.07 \text{ ms}$. As the shock forms so close to the BH formation time, it is even very difficult to detect it as a shock in our numerical simulations. We observe that the region where the classical fundamental derivative is negative does not appear from the beginning in model P-1.9G3. Instead, it appears at $t \simeq 0.01 \text{ ms}$ at $r \simeq 2.8 \text{ km}$, moves radially outwards a few hundred meters (up to $r \lesssim 3 \text{ km}$) and then falls back onto the BH. Also in the latter model the shock formation is slightly delayed with respect to the initiation of the core collapse, though not so much as in model P-1.9G4. In model P-1.9G3 the shock forms sufficiently early to be clearly captured in our simulations.

We point out that the numerical code employed in this section is different from the one used in the next one for reasons we discuss in Section 7. We have repeated the experiments presented in this section with the same fully general relativistic hydrodynamics code with which we obtain the results of Section 6 finding that the qualitative results as well as the quantitative details are nearly the same. This result is reassuring from the methodological point of view since the algorithms implemented in both codes are significantly different. We also consider the independence of the results with respect to the numerical details as a clear hint of their robustness.

6 GRAVITATIONAL COLLAPSE OF ROTATING NEUTRON STARS

In order to study the effects of using our non-convex GGL-EoS in a fully dynamical situation, we consider uniformly rotating neutron star models that are dynamically unstable to axisymmetric perturbations and, hence, collapse to BHs on a dynamical timescale. In the previous section, we have chosen the spherically-symmetric and non-rotating initial data for this purpose. Here, we rather consider the more interesting rotating case since it allows to identify the influence of the non-convex EoS not only on the dynamics of the collapse but *also* on the gravitational-wave signals produced in the process. In particular, we use as initial data two uniformly rotating relativistic star models, dubbed D1 and D4, that have been previously used in a number of numerical-relativity simulations of neutron star collapse (Font et al. 2002a; Baiotti et al. 2005a; Baiotti

Table 2. Uniformly rotating neutron star models with $\gamma = 2$ and $\kappa = 100$. From left to right the columns report the name of the model, the central density ρ_c in code units and in CGS units, the ratio of polar-to-equatorial coordinate radii r_p/r_e , the gravitational mass M_G , and the circumferential equatorial radius R_e .

Model	ρ_c [code units]	ρ_c [g cm ⁻³]	r_p/r_e	M_G M_\odot	R_e [km]
D1	3.280×10^{-3}	2.046×10^{15}	0.95	1.665	11.5
D4	3.116×10^{-3}	1.944×10^{15}	0.65	1.861	14.4
BU2	1.280×10^{-3}	7.984×10^{14}	0.90	1.466	15.0

Table 3. Parameters of the GGL-EoS used in the rotating neutron star collapse simulations.

γ_0	γ_1	σ/ρ_1	ρ_1 [code units]	ρ_1 [g cm ⁻³]
4/3	1.9	1.10	1.5×10^{-3}	9.356×10^{14}
4/3	1.9	1.10	1.7×10^{-3}	1.060×10^{15}
4/3	1.9	1.10 / 1.15 / 1.20 / 1.50	2.1×10^{-3}	1.310×10^{15}
4/3	1.9	1.10	2.5×10^{-3}	1.559×10^{15}

et al. 2007; Giacomazzo et al. 2011). We construct our initial rotating stellar models for a polytropic EoS, $p = \kappa \rho^\gamma$, where $\kappa = 100$ (in code units, where $G = c = M_\odot = 1$) is the polytropic constant and $\gamma = 2$ is the adiabatic index, using the RNS open-access code (Stergioulas & Friedman 1995). The main characteristics of our two models are reported in Table 2. Model D1 is slowly rotating and thus almost spherical, with a ratio of polar-to-equatorial coordinate radii of $r_p/r_e = 0.95$. Correspondingly, model D4 is rotating almost at the mass-shedding limit, with $r_p/r_e = 0.65$. BU2 is a stable model with $r_p/r_e = 0.90$.

The numerical evolution of the initial data entails solving the coupled system of equations given by Einstein's equations, governing the dynamics of the gravitational field, and by the hydrodynamics equations, governing the dynamics of the matter. This is done using the numerical-relativity code in spherical-polar coordinates described in Baumgarte et al. (2013); Montero et al. (2014) and that we have used in previous works (see e.g. Sanchis-Gual et al. 2015, 2017). The Einstein equations are formulated in the so-called BSSN formulation (Baumgarte & Shapiro 1998; Shibata & Nakamura 1995). The evolution equations are integrated using the second-order PIRK method (Cordero-Carrión & Cerdá-Durán 2012; Cordero-Carrión & Cerdá-Durán 2014) which allows to handle singular terms associated with the choice of curvilinear coordinates. The derivatives in the spacetime evolution are computed using fourth-order finite-differences, including fourth-order Kreiss-Oliger dissipation terms to avoid high-frequency noise. The equations of hydrodynamics are formulated in the so-called Valencia formulation (Banyuls et al. 1997) and solved using the second-order MC reconstruction scheme and the HLLC approximate Riemann solver (Montero & Cordero-Carrion 2012). Despite the initial data are built using a polytropic EoS, they are evolved in our code using the GGL-EoS, Eqs. (7-8). As we have tested in the Sec. 5, building a polytropic initial model and then evolving it with the GGL-EoS does not introduce major differences either in the qualitative dynamics, or in the final fate of the collapsing core. It simply results in a *delayed* dynamics, including the time of BH formation.

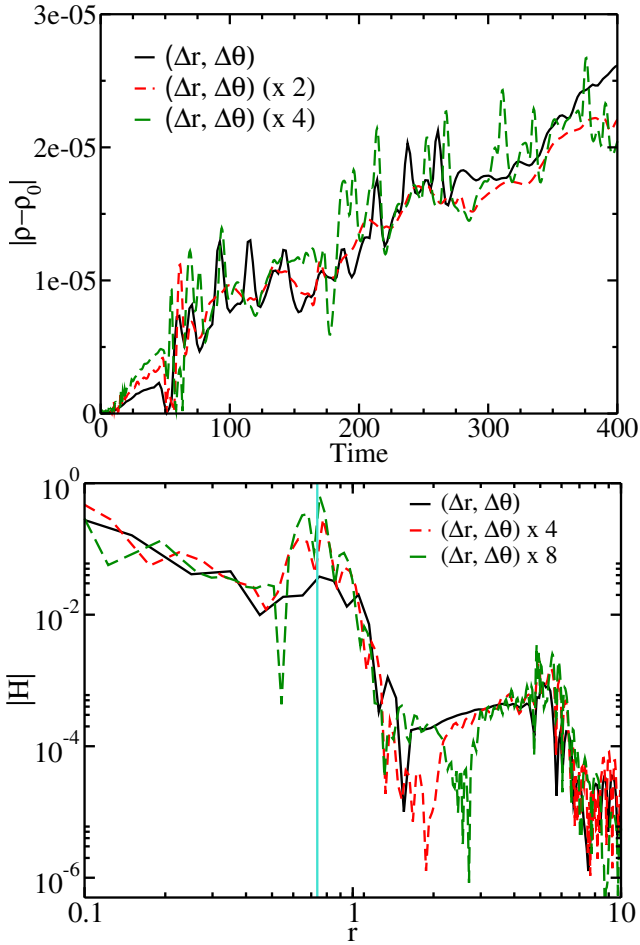


Figure 13. (Top panel): L1-norm of the difference between the evolved rest-mass density and the initial one as a function of time for model BU2. Three different resolutions have been employed. In the legends, we show the minimum radial grid spacings of each of them $(\Delta r, \Delta\theta) = \{(0.05, \pi/16), (0.071, \pi/12), (0.10, \pi/8)\}$. The results corresponding to the finer resolutions are multiplied by the factors of 4 and 2 to show clearly the second order convergence of the method. As in all evolution plots, time is given in “code units”, corresponding to $G = c = M_\odot = 1$. (Bottom panel): Radial profile of the Hamiltonian constraint for model D1 with $\rho_1 = 1.5 \times 10^{-3}$ for three different resolutions $(\Delta r, \Delta\theta) = \{(0.035, \pi/44), (0.05, \pi/32), (0.10, \pi/16)\}$ rescaled to second order convergence. All models have been evolved for a dimensionless time $t = 50$. The snapshot corresponds to the dashed curve in the top right panel in Fig. 16. The vertical cyan line signals the location of the shock wave in model D1 with $\rho_1 = 1.5 \times 10^{-3}$ (Tab. 3). Around the shock location is where the largest (absolute value) violations of the Hamiltonian constraint occur in our models.

The gravitational radiation produced during the collapse of the neutron stars is computed using the Newman-Penrose formalism (Newman & Penrose 1962). More precisely, we compute the so-called Newman-Penrose scalar Ψ_4 , defined by $\Psi_4 \equiv C_{\alpha\beta\gamma\delta} n^\alpha \bar{m}^\beta n^\gamma \bar{m}^\delta$, where $C_{\alpha\beta\gamma\delta}$ is the conformal Weyl tensor associated with the spacetime metric $g_{\alpha\beta}$ and n, \bar{m} are part of a null-tetrad. We use the definition of the electric and magnetic parts of the Weyl tensor, E_{ij} and B_{ij} , as a function of the 3+1 variables evolved by the code, to rewrite the Weyl Ψ_4 scalar as $\Psi_4 = Q_{ij} \bar{m}^i \bar{m}^j$ with $Q_{ij} \equiv E_{ij} - B_{ij}$. We then compute the $l = 2, m = 0$ multipole (which is the dominant mode since the collapse is essentially axisymmet-

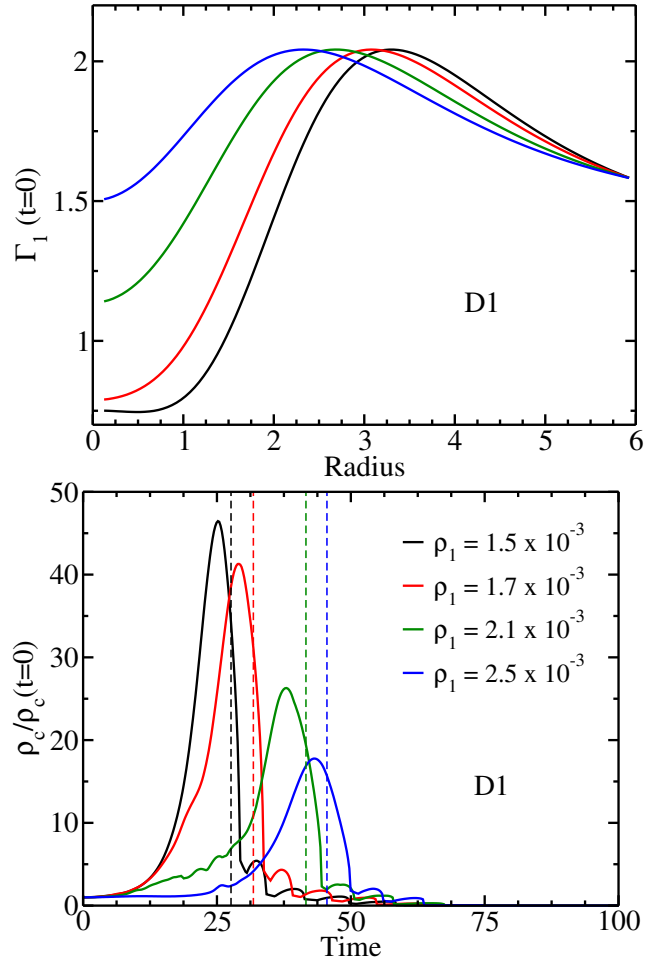


Figure 14. *Top panel:* Initial radial distribution of Γ_1 along the equatorial plane for model D1. *Bottom panel:* Time evolution of the central rest-mass density ρ for model D1. The vertical dashed lines indicate the time at which the apparent horizon forms for each value of ρ_1 . The legend is the same for the two panels.

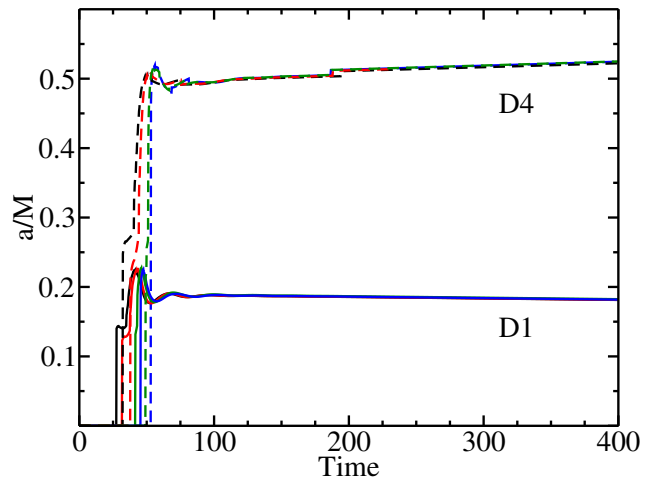


Figure 15. Spins of the final BHs after the collapse of model D1 (solid lines) and model D4 (dashed lines). Each set of four curves corresponds to the four values of ρ_1 in the same colour code as in Fig. 14.

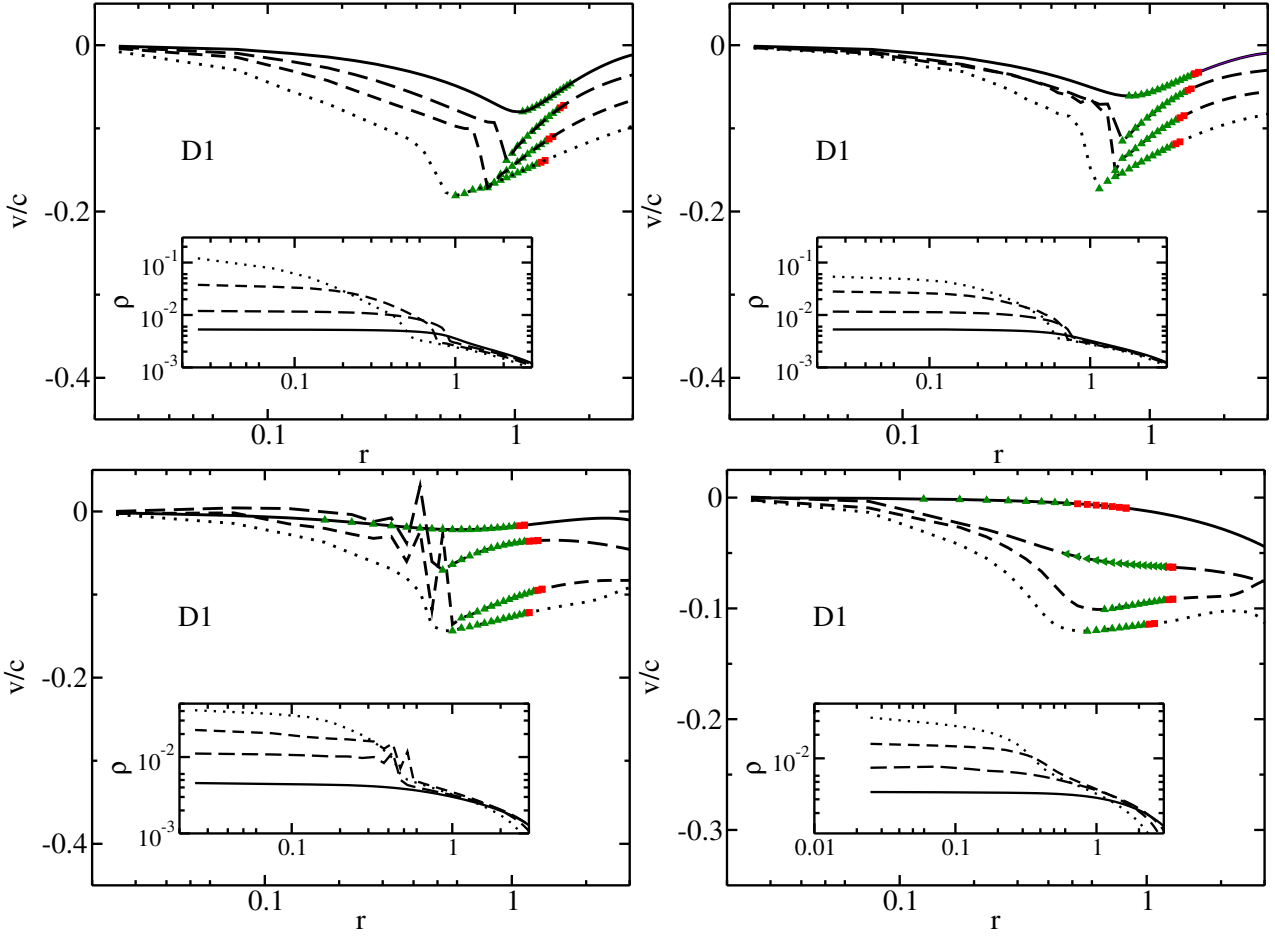


Figure 16. Radial profile of the velocity at the equatorial plane for model D1 at different times of the evolution and for different values of the ρ_1 parameter of the GGL-EoS. Within each panel, the time increases according to the following line style ordering: solid, long-dashed, dashed and dotted. *Top-left panel:* $\rho_1 = 1.5 \times 10^{-3}$, *Top-right panel:* $\rho_1 = 1.7 \times 10^{-3}$, *Bottom-left panel:* $\rho_1 = 2.1 \times 10^{-3}$, *Bottom-right panel:* $\rho_1 = 2.5 \times 10^{-3}$. The insets show the corresponding radial profile of the rest-mass density at the same evolution times as the velocity. Green triangles locate the computational cells where the $\mathcal{G}_{(C)} < 0$ and $\mathcal{G}_{(R)} < 0$, while red squares are drawn for cells where $\mathcal{G}_{(C)} > 0$ and $\mathcal{G}_{(R)} < 0$.

Table 4. Central properties of various models used in the rotating neutron star collapse simulations. $\gamma_0 = 4/3$ and $\gamma_1 = 1.9$ for all models.

Model	σ/ρ_1	ρ_1	ρ_c/ρ_1	p_c/ρ_1
D1	1.10	1.5×10^{-3}	2.187	0.366
D1	1.10	1.7×10^{-3}	1.929	0.387
D1	1.10	2.1×10^{-3}	1.562	0.394
D1	1.10	2.5×10^{-3}	1.312	0.368
D4	1.10	1.5×10^{-3}	2.077	0.356
D4	1.10	1.7×10^{-3}	1.833	0.373
D4	1.10	2.1×10^{-3}	1.484	0.370
D4	1.10	2.5×10^{-3}	1.246	0.339

ric) from

$$\Psi_4(t, \theta, \phi) = \sum_{\ell, m} \Psi_4^{\ell m}(t) {}_{-2}Y_{\ell m}(\theta, \phi), \quad (18)$$

$$\Psi_4^{\ell m}(t) = \int \Psi_4(t, \theta, \phi) {}_{-2}\bar{Y}_{\ell m}(\theta, \phi) d\Omega. \quad (19)$$

where ${}_{-2}Y_{\ell m}$ are the ($s = -2$) spin-weighted spherical harmonics (see, e.g. Thorne 1980).

In order to test the convergence and the gravitational-wave extraction properties of our code we first evolve the *stable* rotating neutron star model BU2 in Table 2 (Stergioulas et al. 2004). Following Font et al. (2002b), we perturb the velocity of the initial model according to

$$u_\theta(t=0) = 0.02 \sin\left(\frac{\pi r}{R_e}\right) \sin\theta \cos\theta, \quad (20)$$

where R_e is the circumferential equatorial radius.

The top panel of Fig. 13 shows the time evolution of the L1-norm of the difference between the evolved rest-mass density and its initial value computed for all the grid points inside the star. The three different curves correspond to three different resolutions, and have been conveniently rescaled to show second-order convergence (see Fig. 13 caption), as expected. We extract the gravitational wave emitted in the evolution of this perturbed model and compute the frequencies of the fundamental quadrupole ($l = 2$) mode, ${}^2f = 1.65 \pm 0.20$ kHz, and its first overtone, ${}^2p_1 = 3.65 \pm 0.20$ kHz. These values are in good agreement with the results obtained in Dimmelmeier et al. (2006).

We next consider the two rotating neutron star models described in Table 2 using different values of the parameters of our

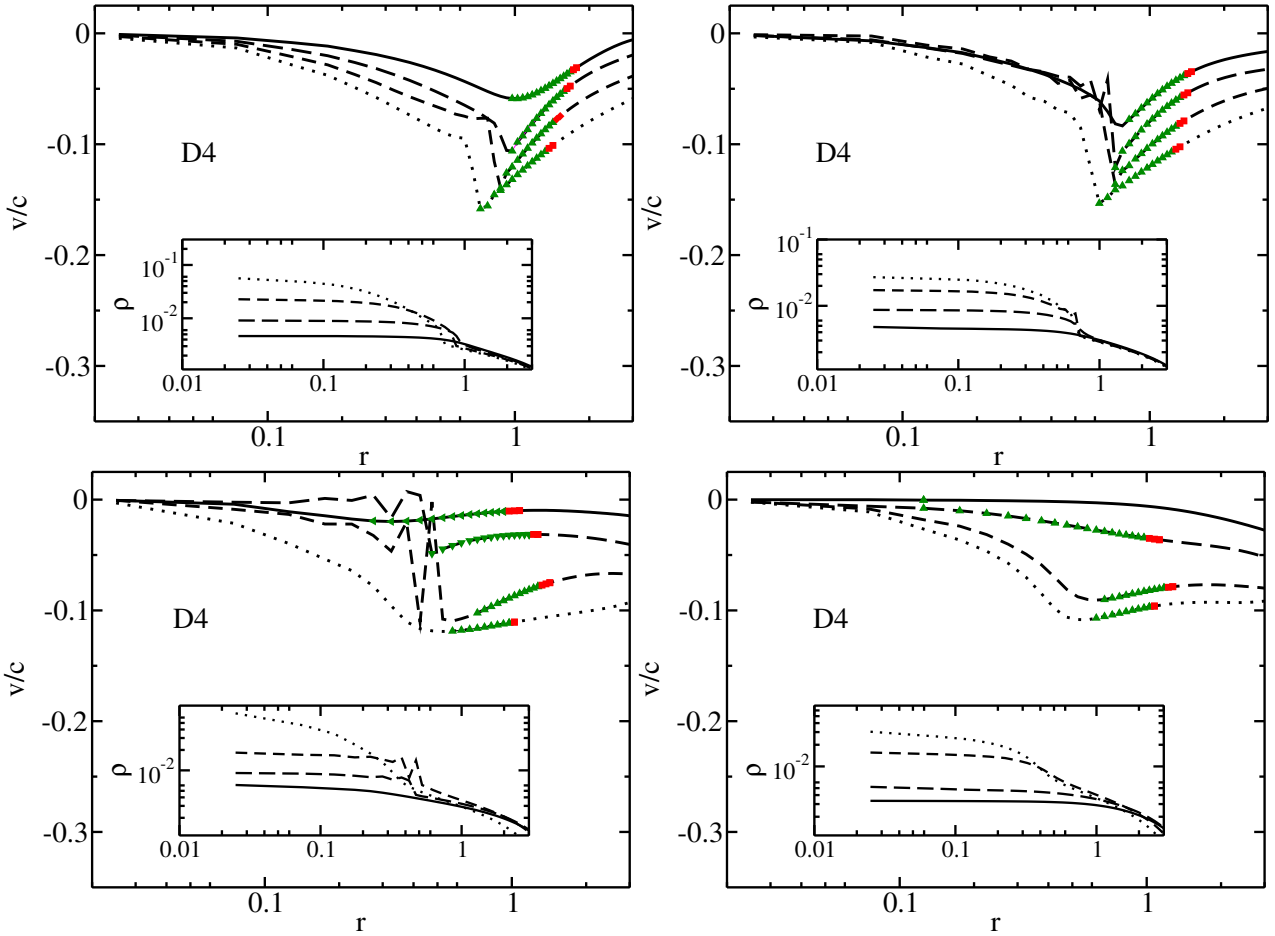


Figure 17. Same as Fig. 16 but for model D4.

phenomenological GGL-EoS. The particular parameters are reported in Table 3. Our simulations are performed in equatorial-plane symmetry. They use a logarithmic radial grid that extends from the origin to $r_{\max} = 600$ and has the finest resolution close to the origin, namely $\Delta r = 0.05$ ($\simeq 74$ m). The angular grid is equally spaced and employs a resolution of $\Delta\theta = \pi/32$. These values for Δr and $\Delta\theta$ have been chosen after a suitable convergence test, but this time comparing the radial distribution of the Hamiltonian constraint at a time where a (bounce) shock has developed in our models (see below). We chose this time since the largest violations of the Hamiltonian constraint are expected to happen in the vicinity of shocks. In the bottom panel of Fig. 13, we plot the radial profile of the Hamiltonian constraint for model D1 with $\rho_1 = 1.5 \times 10^{-3}$. The three different angular resolutions are rescaled to highlight the second-order convergence, almost everywhere, except in the region $0.1 \lesssim r \lesssim 1$. We note that the radial resolution of our best resolved models in 2D is a bit better than that of our 1D models of Sec. 5. However, the 1D models have been computed with a higher spatial and temporal order of accuracy, so that they effectively feature a better resolution. In spite of these small differences, as we shall see (below) the dynamics of two dimensional models with a rough counterpart in the previous spherically symmetric cases is qualitatively the same.

We start by fixing the value of the Gaussian width to $\sigma = 1.1$ and study the effects of varying the parameter ρ_1 . In the top panel of Figure 14 we show the initial radial profile of Γ_1 along the equator

for model D1 and for the different values of ρ_1 we are considering. For later reference, we point out that the set of models D1 with $\rho_1 = \{0.9356, 1.06, 1.31, 1.559\} \times 10^{15} \text{ gr cm}^{-3}$ (Table 3) can be regarded as 2D rotating counterparts of models P-1.9G1, P-1.9G2, P-1.9G3 and P-1.9G4 of Sec. 5 (see Table 1). The non-convex region of the EoS becomes – in radius – larger as ρ_1 becomes smaller, as can be seen from the larger region of non-monotonicity of Γ_1 in the top panel of Fig. 14. The time evolution of the central density of model D1 for the four different values of ρ_1 is shown in the bottom panel. Note that the radius and the time is given in these two panels in code units. The time evolution shows that the smaller the value of ρ_1 , the faster the collapse takes place. This happens because Γ_1 (and also γ) is significantly smaller near the central regions of the star as ρ_1 is reduced (cf. top panel of Fig. 14) and, therefore, the pressure becomes smaller. The time of the formation of the apparent horizon of the BH is indicated in the figure by the vertical dashed lines. We note that BH formation time for models of the series D1 and different values of ρ_1 are about a factor two longer than the values found for models P-1.9G1 to P-1.9G4. The BH formation times in the D1 series range from $t_{\text{BH}} \simeq 27$ to $t_{\text{BH}} \simeq 45$ code units, or equivalently, $t_{\text{BH}} \simeq 0.13$ ms to $t_{\text{BH}} \simeq 0.22$ ms. We attribute the small differences to the rotation present in the 2D models rather than to the approximate treatment of the general relativistic gravitational potential in the AENUS code.

The final outcome is in all cases a rotating Kerr BH whose spin parameter is plotted in Fig. 15. This figure shows that for all the

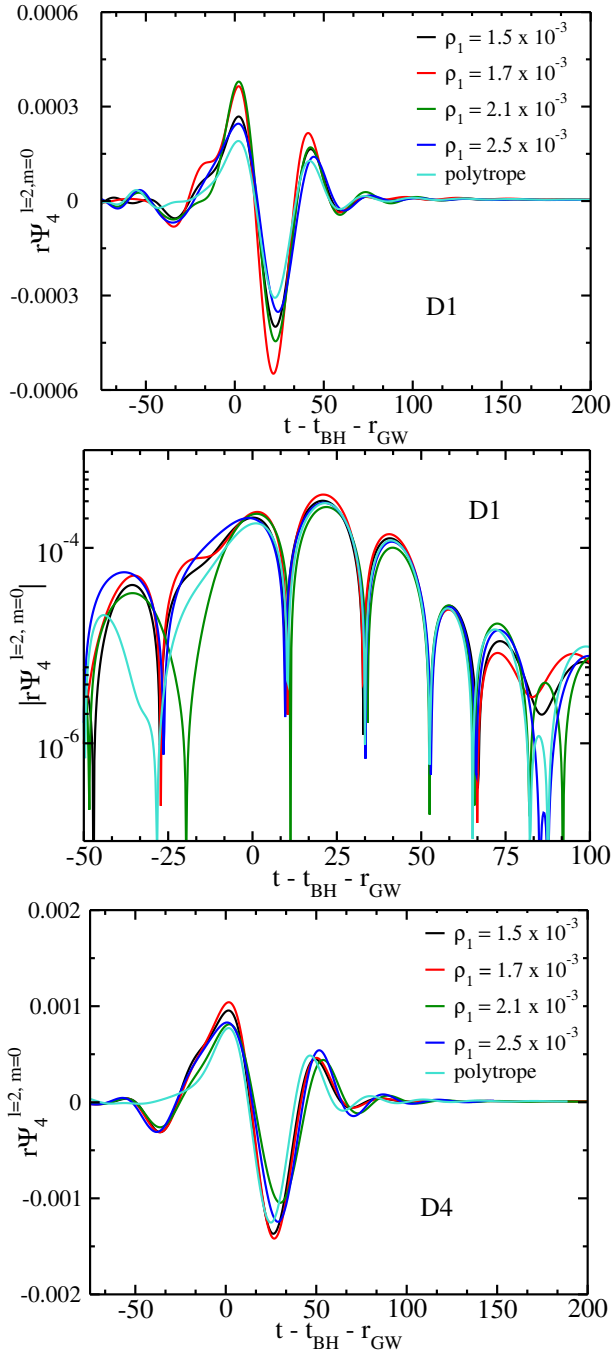


Figure 18. Real part of the ($l = 2, m = 0$) Ψ_4 mode extracted at $r_{\text{GW}} = 200$ for two different RNS models. *Top panel:* model D1. *Middle panel:* log scale of the rescaled gravitational waves for the different values of ρ_1 . *Bottom panel:* model D4. The time axis is given in code units. To convert it to CGS, the reader must multiply the values by $\simeq 4.926 \times 10^{-6}$. For a better comparison, each model time is shifted by its own time of collapse (t_{BH}), defined as the instant when an apparent horizon forms.

unstable models, the final value of the BH spin is fairly independent of ρ_1 . The spin is computed using the expression

$$\frac{a}{M_{\text{hor}}} = \sqrt{1 - (-1.55 + 2.55C_r)^2}, \quad (21)$$

where C_r is the ratio of polar-to-equatorial proper circumference and M_{hor} is the mass of the horizon, which coincides with M when

the spacetime has become axisymmetric and stationary. This expression has an accuracy of $\sim 2.5\%$ (Brandt & Seidel 1995; Baiotti et al. 2005b). The values for the spin and for the irreducible mass with our GGL-EoS differ with those obtained employing a polytropic EoS (Baiotti et al. 2005b) by less than 1%.

In Figs. 16 and 17 we plot the radial profiles of the velocity of the fluid and of the rest-mass density (shown in the insets) for models D1 and D4, respectively. The profiles are plotted at the equatorial plane ($\theta = \pi/2$). The different curves indicate different times during the evolution. The four panels in each of the two figures correspond to the four values of ρ_1 , as indicated in the caption of Fig. 16. We note that for convex EoS, as a polytrope or a gamma-law, the dynamics of the collapse proceeds smoothly towards the formation of a BH, as discussed in Font et al. (2002a); Baiotti et al. (2005a) and we have show in Sec. 5. The larger the centrifugal support of the initial model, the more it takes for the model to collapse. As shown in Baiotti et al. (2005a), the collapse of the rapidly-rotating model D4 goes through a short-lived centrifugal hang-up when the stellar surface slows its inward motion and stalls, although ultimately it shrinks to a volume smaller than that of the radially-increasing event horizon that forms at the central regions. During the evolution of these models, a shock develops at the edge between the homologous inner core of the star and the outer core, which falls supersonically. Consistent with the dynamics observed in the 1D models of Sec. 5, this shock is eventually engulfed by the growing BH that forms as a result of the collapse. For the nearly-spherical D1 model this process is much faster than for the rapidly-rotating model D4. We have also performed the evolutions using an ideal gas EoS, in order to qualitatively compare our findings on the dynamics and on the gravitational-wave emission with the results from these previous works.

It is important to highlight that the formation of the former shock is entirely due to the non-convex dynamics. In the case with $\rho_1 = 2.5 \times 10^{-3}$ (bottom-right panels of Figs. 16 and 17), there is no such shock because for that value of ρ_1 the sound speed in the non-convex region is (much) larger than that of other models with smaller values of ρ_1 . This fact prevents reaching a supersonic regime in the convex region and avoids the formation of the shock. We also point out that for the case with $\rho_1 = 2.1 \times 10^{-3}$ (bottom-left panels of Figs. 16 and 17), and contrary to the two cases displayed in the top panels of both figures, the shock propagates outwards. Furthermore, the flow speed ahead of the shock location is slightly positive. This is due to the *borderline* behaviour of this model, which develops a tiny supersonic region right to the inner radial boundary where the classical fundamental derivative is negative (green triangles in Figs. 16 and 17). This supersonic region persists for a relatively short time along its inner boundary is where the shock forms. We note that the behaviour described for the models D1 with $\rho_1 = 2.1 \times 10^{-3}$ and $\rho_1 = 2.5 \times 10^{-3}$ bears qualitative similarities with the 1D models P-1.9G3 and P-1.9G4, respectively. In model P-1.9G3, we also observe a tiny radial outwards displacement of the shock and the shock formation is significantly delayed with respect to other models of the same series in the case of model P-1.9G4. Thus, we conclude that there is a gross qualitative agreement between the 2D models D1 and their non-rotating counterparts in 1D. The small quantitative differences are almost exclusively induced by the rotation of the former models.

Figure 18 displays the gravitational-wave signals Ψ_4^{20} for models D1 and D4 and for all values of ρ_1 . For the sake of comparison, the three panels of this figure also include additional curves which correspond to a polytropic (convex) EoS. The waveforms are extracted at a radius $r_{\text{GW}} = 200$. For convex EoS, gravitational

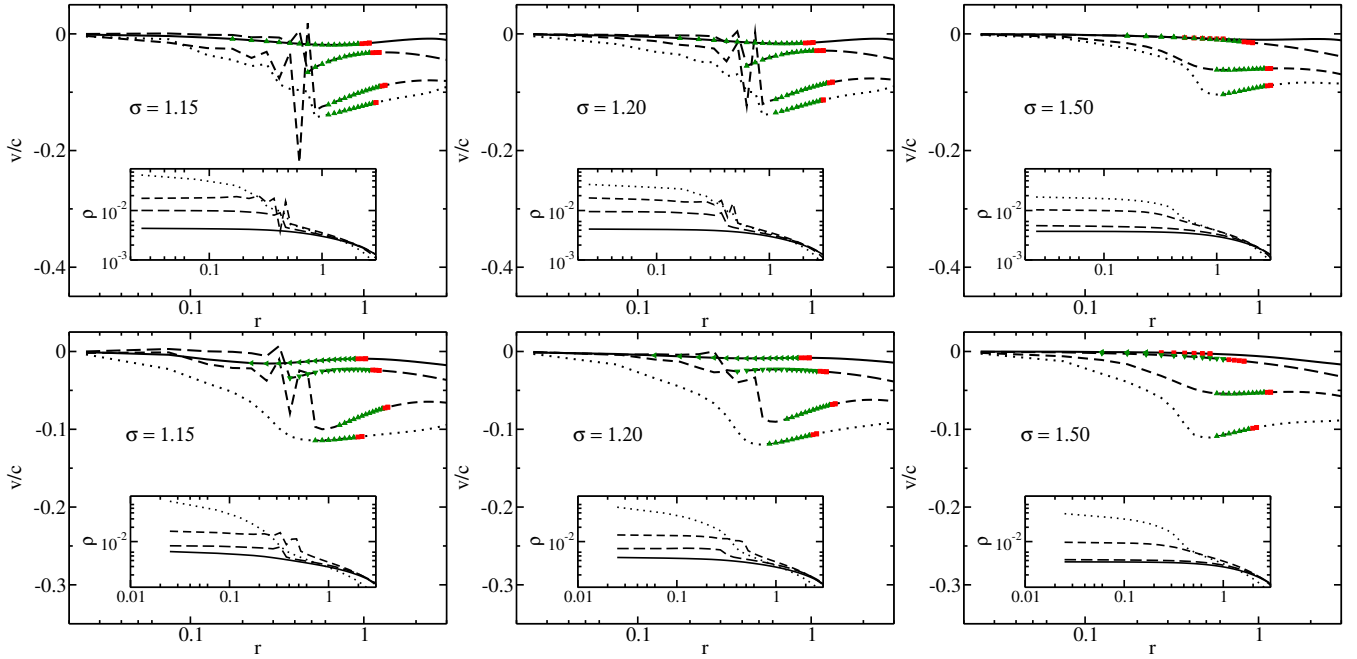


Figure 19. Detail of the radial velocity for different times of models (top panels) D1 and (bottom panels) D4 with $\rho_1 = 2.1 \times 10^{-3}$: Left panels: $\sigma = 1.15$, Middle panels: $\sigma = 1.20$, Right panels: $\sigma = 1.50$.

waveforms of the collapse of these two models have been reported before by Giacomazzo & Perna (2012). The signal is of the burst-type, i.e. it is characterized by an exponential increase of the amplitude and by a short-duration burst at the moment of BH formation (which coincides with the largest positive peak, see Dietrich & Bernuzzi (2015)⁷) followed by the subsequent quasinormal mode ringdown of the BH. Our comparison with the results of Giacomazzo & Perna (2012) for convex EoS shows good agreement in the waveform morphology and amplitude, particularly for model D1 (for model D4 we obtain a few times larger amplitude; note the difference in the vertical scales between the upper and lower panels of Fig. 18).

The non-convex dynamics leaves an imprint in the gravitational waveforms produced during the process. The smallest amplitudes at the moment of BH formation are obtained for the polytropic EoS, specially in the case of model D1 (top panel of Fig. 18). For the GGL-EoS, the frequency of the various signals is quite close to each other, while their amplitudes are different depending on the value of ρ_1 . This is more apparent for model D1 than for model D4. In the case of model D1 in particular, the largest gravitational-wave amplitude is obtained for $\rho_1 = 1.7 \times 10^{-3}$ (red curve in the top panel of Fig. 18). The maximum amplitude is about twice that attained in the polytropic case. For model D4 the maximum amplitude is also achieved for the same value of ρ_1 but the differences among the various simulated models are not as apparent as for model D1. This means that the faster the rotation of the initial neutron star, the smaller the imprint the loss of convexity leaves on the gravitational-wave signal after the BH has been formed.

The radially outwards propagation of the shock in model

D1 with $\rho_1 = 2.1 \times 10^{-3}$ (Fig. 16) translates in slightly higher gravitational-wave amplitudes at the time of collapse, but slightly smaller in the instants preceding the BH formation. The speed of this outgoing shock is smaller than the speed at which the BH horizon grows and eventually all neutron star matter will be inside of the BH. This can be inferred from the middle plot of Fig. 18 which displays the (absolute value of) the gravitational waveforms of model D1 in logarithmic scale. We note that the curves in this figure have been conveniently shifted in time in order to synchronise the time of BH formation. Later, after the amplitude reaches a minimum, all of the infalling matter has been captured by the BH, whose area stops growing. Irrespective of the thermodynamical details of the collapse, encoded in our phenomenological EoS by the different values of the ρ_1 parameter, the final Kerr BH must have the same mass and angular momentum, as implied by the fact that all four gravitational-wave signals have the same frequency and exponential decay, associated with the distinctive quasinormal mode ringdown signal of a BH. We observe, however, that the largest discrepancies among different models happen in the pre-collapse phase ($t - t_{\text{BH}} - r_{\text{GW}} < 0$ in Fig. 18). There, we see that the fingerprint of convexity loss in the course of the collapse is an increasing spectral power and amplitude in the pre-collapse phase of model D1 compared to a polytropic model (which would be representative of a collapse developed with a fully convex EoS; cyan line in the top and central panels of Fig. 18).

The waveforms shown in the bottom panel of Fig. 18 correspond to model D4. In this case, the maximum amplitudes of the burst signals are significantly larger than in the case of model D1, and for all values of ρ_1 , the reason being the increased deviation from spherical symmetry of this rapidly-rotating model. While model D4 displays more similar gravitational waveforms for all values of ρ_1 than model D1, when comparing with the polytropic EoS there is still a visible change in frequency associated with the non-convexity properties of the GGL-EoS. This is particularly ev-

⁷ Notice that Giacomazzo & Perna (2012) associate the first negative peak to the moment of BH formation due to a global sign difference in the expression of Ψ_4 they use compared to ours and Dietrich & Bernuzzi (2015).

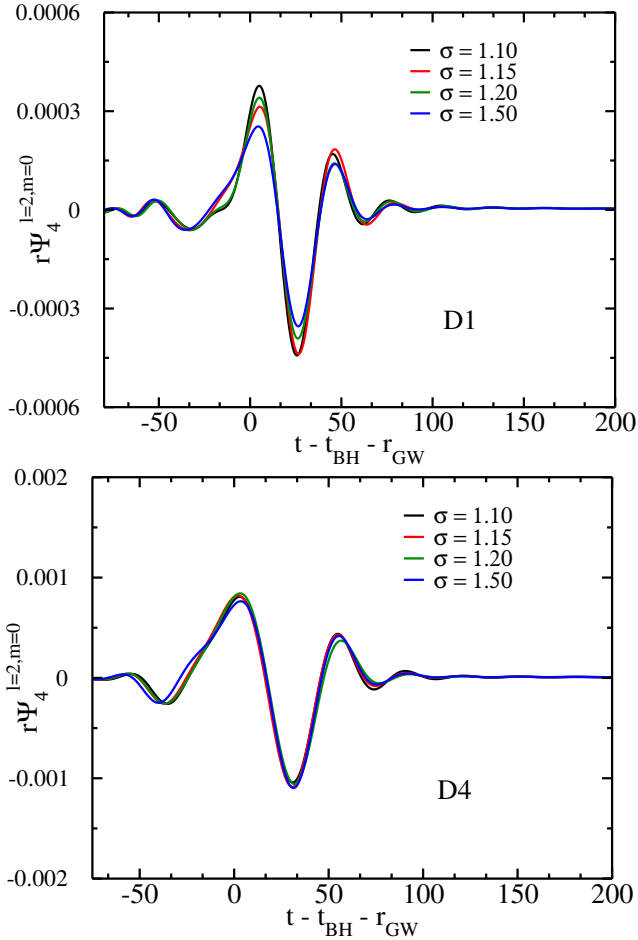


Figure 20. Real part of the ($l = 2, m = 0$) Ψ_4 mode for the model D1 (top) and D4 (bottom) with $\rho_1 = 2.1 \times 10^{-3}$.

ident in the first part of the signal associated with the collapsing phase before the BHs form.

Additionally, we also study the effects of varying the width σ of the Gaussian used in the definition of the GGL-EoS, fixing $\rho_1 = 2.1 \times 10^{-3}$. We analyze the dynamics of the collapse for four different values of σ , namely $\{1.10, 1.15, 1.20, 1.50\}$. The results for models D1 and D4 are displayed in Fig. 19, which depicts the radial profile of the fluid velocity at the equatorial plane. As we have shown before, for this value of ρ_1 the shock located in the region $0.2 < r < 0.9$ attains a slightly positive speed if $\sigma \lesssim 1.20$. The jumps at the latter shock become gradually smaller when σ increases from 1.10 (see Fig. 16) to 1.20. For $\sigma = 1.50$ the shock is no longer visible and the dynamics resembles that of a convex EoS. This trend is the same for both models, i.e. it does not depend on the initial rotation of the unstable neutron star.

The corresponding gravitational waveforms are shown in Fig. 20. The waveforms look remarkably similar irrespective of the value of σ , with minor differences in the peak amplitudes among all models. As in the cases previously analyzed, the waveforms of the most rapidly rotating models D4 are less sensitive to the changes in σ than in models D1.

7 SUMMARY AND OUTLOOK

A number of microphysical EoSs of high-density matter contain regions in which the thermodynamics may be non-convex. These EoSs, commonly used in a tabular form, may develop non-convex thermodynamics either as a result of first-order PTs (regardless of whether they are congruent or non-congruent), or non-consistent treatment of the matter constituents (non-relativistic instead of relativistic), or specific parameter sets in the RMF theoretical framework. In the first group we find EoSs where transitions from nuclear hadronic matter into quark-gluon plasma or into matter phases containing exotic particles (e.g. hyperons) are included employing suitable Gibbs constructions. The second group gathers EoSs in which baryons are treated as non-relativistic particles. A prototype example of the latter group is the LS220 EoS. To the third group belong EoSs which include the NL3 parameter set in the RMF treatment. However, other parameterizations of the RMF (e.g. FSU2) are convex in the classical sense (i.e. $\mathcal{G}_{(C)} > 0$) even at high number densities.⁸ The NL3 RMF parameterization yields a clean and genuinely relativistic situation, namely, the large magnitude of the sound speed drives negative values only of the relativistic fundamental derivative, but the classical fundamental derivative remains positive (i.e. $\mathcal{G}_{(R)} < 0$ and $\mathcal{G}_{(C)} > 0$) for sufficiently large number densities ($n \gtrsim 0.8 \text{ fm}^{-3}$). This is clearly observed in the HS (NL3) EoS at both $s = 0.5$ and $s = 2.5$, as well as in the GSHen (NL3) at $s = 0.5$ (at higher entropies per baryon we do not have available thermodynamical data to confirm this point, but clearly both equations should behave qualitatively in the same way at sufficiently large number densities and entropies). In light of the latest developments for the constituents of the merger GW170817 (Abbott et al. 2017e, 2018), we point out that the NL3 parameterization may be too stiff, giving in particular too high values for the tidal deformability, the neutron star radii and the slope of the symmetry energy if one assumes low spin priors for the merging objects (see, e.g. Malik et al. 2018). In any instance, a good number of the studied microphysical EoSs display a sensitive reduction of the relativistic fundamental derivative as the baryon number density grows above $n \gtrsim 1 \text{ fm}^{-3}$. In that regime ($n \gtrsim 1 \text{ fm}^{-3}$; $\mathcal{G}_{(R)} \gtrsim 0$), even small scale oscillations of numerical origin, namely due to the discretization of high-order derivatives across coexistence boundaries in PTs, may be enough to *drive* ($\mathcal{G}_{(R)} \lesssim 0$). Since small scale oscillations in the evaluation of high-order derivatives are *hardly avoidable* in tabular representations of dense-matter EoS (broadly used in computational astrophysics), and since the EoS at number densities above 1 fm^{-3} is poorly constrained, we warn that physical, but most likely *numerical*, non-convex thermodynamics may develop in that regime. We note, however, that the convexity across first-order PTs may be numerically recovered. Some times (but not in all cases), the singularities exhibited by the Gibbs (or Helmholtz) free energy are removable singularities. Thermodynamical consistency requires that the Gibbs free energy be a jointly concave function. This requirement may be enforced convolving the Gibbs free energy with a non-negative smoothing function, which mollifies the singularities at phase transitions (c.f. Menikoff & Plohr 1989). The physical and mathematical conditions required to undertake such convexity recovery are beyond the scope of this paper, but may be the subject of a future work.

Unfortunately, most available microphysical EoSs are only

⁸ The negative values observed for $\mathcal{G}_{(C)}$ in the GSHen (FSU1) case at high number densities are likely numerical artifacts (see App. A).

tabulated up to baryon number densities $n \lesssim 3 \text{ fm}^{-3}$, making it difficult to assess whether convexity will be lost at high enough baryon number density. Hopefully the present work will spark an interest in this question, by pointing the phenomenological consequences that such a non-convex regime would have. Adding to these arguments, we point out the non-monotonic behaviour of the sound speed in dense matter found by Bedaque & Steiner (2015), which is a strong hint on the non-convex character of matter at high densities. Remarkably, Bedaque & Steiner (2015) found that the more abrupt the sound speed changes with density (from its values at $n = 2n_0$ to the asymptotic value $1/\sqrt{3}$) the larger are the maximum masses of neutron stars they can build within their model (near $2M_\odot$). This non-monotonic behaviour of the sound speed may occur (depending on the EoS) at baryon number densities within reach of the maximum values of the number density predicted for *ordinary* neutron stars (namely, 5 – 8 times the nuclear saturation density for most EoS of dense matter) as well as in hybrid stars containing a quark phase (see e.g., Bonanno & Drago 2009; Alford et al. 2013). Indeed, we have shown an example of a hadronic EoS that contains the transition to quark matter in the above mentioned density range (the case of $\text{CMF}(\Lambda\text{B})$), which displays a significant decrease of the sound speed and satisfies the existing astrophysical and experimental constraints. Connecting Bedaque & Steiner (2015) results with ours could suggest that neutron stars or hybrid stars with masses above $\sim 2M_\odot$ (if hyperons are included as possible degrees of freedom this limit may be a bit smaller; see below) may have undergone a phase during their formation, either at bounce or on longer (post-bounce) time scales where thermodynamics could have been non-convex. This possibility strongly depends on whether the non-monotonic behaviour of the sound speed also drives a negative fundamental derivative, i.e. it depends on the EoS as well as on other additional dynamic effects as, e.g. whether the stellar core is strongly rotating. The reason for it is that it is necessary to significantly exceed nuclear saturation density in order to reach the regime in which non-monotonicity of the sound speed (and hence, a possible convexity loss) may happen. During the dynamical phase of stellar collapse, the maximum number densities are reached just at bounce and these can be $\sim (2 - 3) \times n_0$ (e.g. Dimmelmeier et al. 2008). Later, on longer time scales, the density of the proto-neutron star increases as it contracts and cools down (e.g. Sumiyoshi et al. 2005; Suwa 2014), though the central density only experiences very little increments on time scales of $\sim 20\text{s}$ (Fischer et al. 2010) except if matter also contains hyperons. In this case the central number density may increase (within less than 100 s post bounce) and reach values $n \simeq 0.85 \text{ fm}^{-3}$ for a proto-neutron star with mass $\simeq 1.79M_\odot$ (see Fig. 22 in Pons et al. 1999). Thus, if hyperons are present it is much more likely to eventually reach a non-convex region (in some EoS) in the post-bounce phase than right at bounce.

Indeed, the above mentioned ultra-high densities are of interest when the final fate of the collapse of stellar cores or binary neutron star mergers is the formation of a BH. This is, for instance, the case of metastable proto-neutron stars having a hyperon phase in the core and baryonic masses $\gtrsim 1.8M_\odot$. Unless fine-tuned parameters of the hyperon-hyperon interaction are considered, these configurations undergo a BH collapse on time scales of $\lesssim 100\text{s}$, during which they may build a central number density $\simeq 3 - 4 \text{ fm}^{-3}$ (Pons 1999), improving the prospects of finding a non-monotonic behaviour of the sound speed and a potential convexity loss. An extension of the available microphysical EoSs beyond the current upper boundaries in baryon number density is needed to thoroughly

explore any potential non-convex regime happening before the formation of the apparent horizon.

In this paper we have presented a numerical study of the structure, dynamics and gravitational-wave signature of compact stellar configurations described by a BZT fluid. Missing the appropriate extensions of tabular microphysical EoSs to explore the ultra-high density regime, we have resorted to a simple, phenomenological, non-convex EoS, which mimics some of the qualitative properties that microphysical EoSs possess. This ideal-gas-like EoS holds a density-dependent adiabatic index (or similarly, a non-monotonic sound speed dependence with density) and a causal behavior within a broad range of EoS parameters. The reason behind our simplistic choice of such a toy-model EoS has been to provide a proof-of-concept of the peculiarities associated with non-convex EoS before attempting further work employing state-of-the-art, microphysical EoSs.

We have studied the dynamics triggered by the non-convexity of the EoS analyzing three different situations. First, the equilibrium structure of stable compact stars. Second, the collapse of spherically symmetric neutron stars to BHs. Third, the dynamics of unstable and uniformly-rotating neutron stars that collapse gravitationally to BHs on a dynamical timescale. The numerical simulations have been performed with two different codes, which guarantees the numerical robustness of our results. We have used the most basic HLL solver to prevent a breach in our simulations that may happen between adjacent numerical zones across which the fundamental derivative changes sign as it is the case of the (S)GGL-EoS. For the fluid flow system of equations closed with a non-convex EoS, it has been demonstrated that if the approximate Riemann solver provides a sufficient amount of numerical viscosity to allow the formation of compound waves, the resulting numerical method is stable (see Argrow 1996; Guardone & Vigeveno 2002; Voss 2005; Cinnella & Corre 2006; Serna & Marquina 2014). In particular, the HLL approximate Riemann solver satisfies the above requirements in relativistic fluid dynamics (Ibáñez et al. 2018).

The numerical simulations of collapsing stars have shown the appearance of non-convex dynamics. Remarkably, the non-convexity of the dynamics does not result in compound waves (e.g. rarefaction shocks or compressive rarefactions). This result is somewhat unexpected in view of the fact that our models produce BZT fluids, which may develop anomalous dynamics (see, e.g. Ibáñez et al. 2018). Instead, the new dynamics produced by the non-convexity of our phenomenological EoS stems from the non-monotonic dependence of the sound speed with density. As a result, regions where the sound speed decreases significantly form in the course of the collapse. In these regions the infalling matter becomes *suddenly* supersonic and a shock forms. This shock is not expansive as one may guess, since it is produced as a result of the development of a non-convex region in the collapsing core. Noteworthy, all shock structures developed during the infalling phase are engulfed by the nascent BH. This result holds independent of whether the initial neutron star is rotating or it is spherically symmetric. To our knowledge, the behaviour we have found in our models has some precedent even using a microphysical EoS. Calculations of collapsing proto-neutron stars with a kaon condensate also showed the formation of an accretion (compression) shock in Pons (1999). That feature was attributed to the fact that $dp/dn = 0$ in the region where the Maxwell construction for the PT was used. Pons (1999) argued that a different treatment of the PT (e.g. employing a Gibbs rather than a Maxwell construction) would have prevented the formation of discontinuities, keeping finite the compressibility. While this conclusion is correct, we also note that the treatment of PTs

in nuclear matter is an active field of research. So far, there is no global consensus in the Nuclear Physics community on, e.g. how to properly treat the transition from inhomogeneous to homogeneous nuclear matter. Therefore, we signal in this paper the potential consequences of a convexity loss in the dynamics due to the loss of convexity especially in first-order PTs.

The existence of regions where the fundamental derivatives are negative is imprinted on the gravitational-wave signals associated with the infalling phase. Furthermore, the increased amplitude of the gravitational waves in the phase immediately preceding BH formation might be the only signature of a non-convex dynamics, unless a successful SN explosion is driven as a result of the released latent heat of a first-order PT (this is the case of the hadron-quark PT in, e.g. Sagert et al. 2009; Fischer et al. 2018). If the SN fails, electromagnetic signals of this phase are not foreseen since the system is extremely optically thick to radiation in the regime in which convexity is lost. Likewise, neutrino emission is unimportant inasmuch as neutrinos are fully trapped inside the collapsing neutron star. However, neutrinos may act as a source of physical viscosity in the system (Guilet et al. 2015, 2017). Therefore, they may smooth out the shocks developed in the limits of the non-convex regions formed in the course of the collapse, and hence, they may wash out any prominent effect of the convexity loss in the course of the collapse dynamics. A future study using actual microphysical EoS from nuclear physics and a suitable neutrino transport is opportune and will be presented elsewhere. In a different context that we have addressed here, we point out that Most et al. (2018a) have already found a systematic dephasing of the GW emission after the merger of two neutron stars, which may produce a qualitatively distinct signature in the post-merger GW signal and spectrum. These authors further conclude that the inclusion of a first-order PT to quark matter significantly accelerates the collapse to BH of the post-merger remnant and changes the ringdown GW frequencies. We point out that, since the transition to quark matter of first-order kind in the variant of the CMF EoS that Most et al. (2018a) have used (corresponding with the CMF (Λ B) EoS), the convexity shall be lost in their merger models (as we have shown here). Therefore, the strong impact of the GW signature that they find, is also an indirect trace of the convexity loss at densities a few times larger than the nuclear saturation density. Furthermore, we note the qualitative resemblance of their results with ours: a significant modification of the GW emission is found after the, essentially, free-fall collapse of an unstable neutron star remnant.

As a final note, we want to convey the idea that a finer tabulation of nuclear matter EoSs is probably adequate when the fundamental derivative displays large variations, specially, when these variations drive negative values of $\mathcal{G}_{(C)}$. This means that, for applications in Computational Astrophysics it is probably worth including additional tabular points in situations where $\mathcal{G}_{(C)} < 0$. This means mapping with more tabular points thermodynamical states near the boundaries of regions where Maxwell or Gibbs constructions are built to deal with first-order PTs.

APPENDIX A: NUMERICAL ARTIFACTS IN THE EVALUATION OF FUNDAMENTAL DERIVATIVES

We have investigated whether the differences between distinct variants of the LS220 EoSs (including cases with Λ hyperons) may arise due to the distinct tabulation resolution. For the LS220 EoS, the three-dimensional table in (T, n, Y_q) obtained from the CompOSE webpage, where n and Y_q are the baryon number den-

sity and the charge fraction, respectively, contains (163, 164, 51) points logarithmically allocated along the T - and n -directions of the table and linearly collocated in the Y_q -direction, covering the ranges $0.1 \text{ MeV} \lesssim T \lesssim 182 \text{ MeV}$, $5.2 \times 10^{-8} \text{ fm}^{-3} \lesssim n \lesssim 12 \text{ fm}^{-3}$ and $0.03 \lesssim Y_q \lesssim 0.5$. For the HS EoS, the tables contain (81, 326, 60) points to cover the intervals $0.1 \text{ MeV} \lesssim T \lesssim 158 \text{ MeV}$, $10^{-12} \text{ fm}^{-3} \lesssim n \lesssim 10 \text{ fm}^{-3}$, $0.01 \lesssim Y_q \lesssim 0.6$ and, as a result, the temperature resolution is about twice better in the LS220 tables than in the HS ones, while the baryon number density resolution is only $\sim 20\%$ better in the HS tables than in the LS220 case. In order to compute the fundamental derivative using numerical derivatives along the tabular directions we employ the expression

$$\mathcal{G}_{(C)} = 1 + \left. \frac{\partial \ln c_{s(C)}}{\partial \ln n} \right|_{T, Y_q} + \frac{\beta_V}{nc_V} \left. \frac{\partial \ln c_{s(C)}}{\partial \ln T} \right|_{n, Y_q}, \quad (\text{A1})$$

where, β_V is the tension coefficient at constant volume

$$\beta_V = \left. \frac{\partial p}{\partial T} \right|_{n, Y_q}, \quad (\text{A2})$$

and c_V is the specific heat capacity at constant volume

$$c_V = \frac{T}{n} \left. \frac{\partial s}{\partial T} \right|_{n, Y_q}. \quad (\text{A3})$$

For the calculation of the derivatives involved in $\mathcal{G}_{(C)}$ and $\mathcal{G}_{(R)}$, the resolution in number density is more important than in the other two directions. Thus, a priori, we may guess that a finer number density resolution across the PT should provide smoother results and, if the negativity of the fundamental derivatives would come from a purely numerical origin, the expectation would also be that the fundamental derivative would remain positive for finer number-density discretizations too. However, this is not the case and the HS EoS displays a more oscillatory behaviour of the fundamental derivatives.

Restricting our attention to the LS220 EoS, we have compared the fundamental derivatives obtained with different tabulations (i.e. different tabular nodal points) and numerical computation of the thermodynamic derivatives. For that, we have employed two tabular versions of the LS220 EoS built by O'Connor & Ott (2010) in addition to the two variants obtained from the CompOSE web page shown before. The table dubbed LS220hr (O'Connor & Ott 2010) possesses a resolution in number density and charge fraction that is roughly the same as in the CompOSE tables (19.5 points per decade for the number density and 50 uniform points for Y_q), while the temperature resolution ($\simeq 38$ points per decade) is slightly worse than in the CompOSE tables ($\simeq 50$ points per decade). The other LS220 variant (tagged LS2201r; O'Connor & Ott 2010) has a poorer resolution in temperature ($\simeq 30$ points per decade) and number density ($\simeq 18$ points per decade) than the LS220hr table. It is evident from Fig. A1 that $\mathcal{G}_{(R)} < 0$ through the PT in the tabular versions of the LS220 EoS which do not include hyperons (LS220, LS220hr and LS2201r). All these variants of the LS220 EoS have been broadly used in actual calculations of stellar core collapse and supernovae (e.g. Couch & Ott 2013; Couch & O'Connor 2014) and, necessarily, these computations have accessed the regime where the transition from non-uniform to uniform nuclear matter is located. Thus, it is very likely that state-of-the-art models of supernovae have included regions of the thermodynamics phase space which are non-convex (due to the particular realization of the PT under consideration). We note that since the tabulation of the tables LS220hr and LS2201r is done as a function of (T, n, Y_q) , we do not show in Fig. A1 the relativistic fundamental derivative along an isentrope

(as was done in Figs. 2 and 3), but along a curve of constant temperature and charge fraction. This explains why the LS220 (Λ) EoS does not display $\mathcal{G}_{(R)} < 0$ in this case, while it does it for the isentrope $s = 2.5$ (Fig. 3).

Regardless of the discretization of the tables, which may induce spurious changes of sign of the fundamental derivatives, across the PT, Hempel & Schaffner-Bielich (2010) stated that discontinuities of the second derivatives of the Helmholtz free energy result from the enforced Maxwell construction, which we remind is the same as used in the LS220 EoS. This is the physical root of the large amplitude oscillations and changes of sign of the fundamental derivative in both the HS EoS and the LS EoS without the incorporation of hyperons. In contrast, the LS220 (Λ) EoS, was constructed by Oertel et al. (2012), who took special care in fixing a number of pathologies of the PT under consideration. The result are positively defined fundamental derivatives across the PT in the latter EoS and the conditions considered here. Remarkably, the EoS of Oertel et al. (2012) employs also a Maxwell construction to deal with both the PT from inhomogeneous to homogeneous nuclear matter as well as the transition to the hyperon phase.

Another place where numerical artifacts (associated to the calculation of high-order derivatives) may exist is close to the tabular boundaries. This seems to be the case in the GSHen EoS, which displays different behaviors depending on the RMF parameterization at low entropies. While the original FSUGold or FSU1 parameterization included in the GSHen (FSU1) EoS shows large amplitude oscillations, where both the relativistic and classical fundamental derivatives become negative at high density ($n \gtrsim 1 \text{ fm}^{-3}$) and low entropies per baryon (Fig. 2), the FSU2 and NL3 parameter sets (corresponding to GSHen (FSU2) and GSHen (NL3), respectively) are classically convex (i.e. $\mathcal{G}_{(C)} > 0$) up to the highest baryon density at which they are tabulated, i.e. $n_{\text{max}} \simeq 1.5 \text{ fm}^{-3}$. As we have anticipated above, the convexity loss of the GSHen (FSU1) EoS is likely due to numerical artifacts in the computation of high-order thermodynamic derivatives near the table boundaries. Large amplitude oscillations at high number densities are not observed at higher entropies per baryon ($s = 2.5$) because the CompOSE tables of the GSHen EoSs do not contain tabular points at sufficiently large temperature to compute values of the thermodynamic quantities along the isentrope $s = 2.5$ for $n \gtrsim 0.6 \text{ fm}^{-3}$ (Fig. 3; upper row).

APPENDIX B: ANALYSIS OF THE ‘PolyTh’ EOS

A simple way to mimic the complex thermodynamical processes taking place inside a collapsing stellar core in simulations of hydrodynamical supernovae and in the formation of compact objects, considers an EoS for which the pressure has two components, namely a polytropic component (the cold one, p_c), and an ideal-gas component which incorporates the thermal effects p_t . This EoS, that we call ‘PolyTh’ reads as (see, e.g. Maione et al. 2016)

$$p = p_c + p_t, \quad p_c = K \rho^{\Gamma_c}, \quad p_t = (\Gamma_t - 1) \rho \varepsilon_t, \quad (\text{B1})$$

where

$$\varepsilon_t = \varepsilon - \varepsilon_c, \quad \varepsilon_c = \varepsilon_0 + \frac{K}{\Gamma_c - 1} \rho^{\Gamma_c - 1}. \quad (\text{B2})$$

The total specific internal energy ε , or its thermal component ε_t , can be considered as an independent thermodynamical variable, being the cold component ε_c a function of density given by Eq. (B2). In practice, we take ε_0 , in Eq. (B2), equal to zero. The free parameters of the PolyTh-EoS are K, Γ_c and Γ_t .

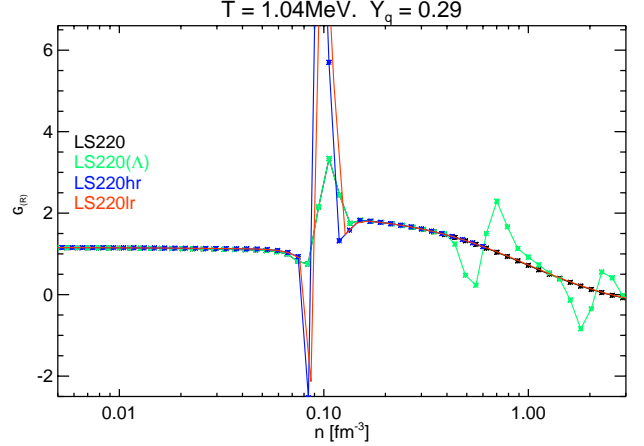


Figure A1. Comparison of different tabular versions of the LS220 EoS. We fix the same temperature and charge fraction as in Fig. 2 and consider the two versions of the LS220 EoS obtained from the CompOSE web page (LS220 and LS220 (Λ)) in addition to the *high-* and *low-resolution* tables from <https://stellarcollapse.org/equationofstate>, respectively labeled LS220hr and LS220lr. We note that the plot of the relativistic fundamental derivative corresponding to the LS220hr falls on top of the one corresponding to the LS220 EoS in the number density range where both tables overlap.

Let us define

$$a_\alpha^2 := \Gamma_\alpha \left(\frac{p_\alpha}{\rho} \right) = \Gamma_\alpha (\Gamma_\alpha - 1) \varepsilon_\alpha \quad (\text{B3})$$

where $\alpha (= c, t)$ stands, respectively, for the cold and thermal components of pressure. Hence, the classical definition of the local speed of sound can be written

$$c_{s(c)}^2 = a_c^2 + a_t^2. \quad (\text{B4})$$

The specific enthalpy is given by

$$h := 1 + \varepsilon + \frac{p}{\rho} = 1 + \Gamma_c \varepsilon_c + \Gamma_t \varepsilon_t, \quad (\text{B5})$$

or, alternatively,

$$h = 1 + \frac{a_c^2}{\Gamma_c - 1} + \frac{a_t^2}{\Gamma_t - 1}. \quad (\text{B6})$$

The relativistic definition of the speed of sound is related to the classical one according to:

$$c_{s(R)}^2 = h^{-1} c_{s(c)}^2 = \frac{\Gamma_c (\Gamma_c - 1) \varepsilon_c + \Gamma_t (\Gamma_t - 1) \varepsilon_t}{1 + \Gamma_c \varepsilon_c + \Gamma_t \varepsilon_t}. \quad (\text{B7})$$

From this equation we obtain the following constraint that the PolyTh EoS has to satisfy in order to be causal:

$$c_{s(R)}^2 \leq 1 \implies \Gamma_c (\Gamma_c - 2) \varepsilon_c + \Gamma_t (\Gamma_t - 2) \varepsilon_t \leq 1. \quad (\text{B8})$$

Hence, assuming that both ε_c and ε_t are non-negative, a sufficient condition for causality is

$$\Gamma_c \leq 2 \quad \text{and} \quad \Gamma_t \leq 2 \quad (\text{B9})$$

There are a critical values of $\varepsilon_c^{\text{crit}}$ and $\varepsilon_t^{\text{crit}}$, at the stationary point of $c_{s(R)}^2$

$$\left. \frac{\partial c_{s(R)}^2}{\partial \varepsilon_\alpha} \right|_{\varepsilon_\beta} = 0 \implies \varepsilon_\alpha^{\text{crit}} = \frac{\Gamma_\alpha - 1}{\Gamma_\beta (\Gamma_\beta - \Gamma_\alpha)} \quad (\alpha \neq \beta). \quad (\text{B10})$$

By definition, the adiabatic exponent, Γ_1 , is

$$\Gamma_1 = \left(\frac{\rho}{p}\right) c_{s(C)}^2 = \left(\frac{\rho}{p}\right) (a_c^2 + a_t^2), \quad (\text{B11})$$

or, alternatively

$$\Gamma_1 = \Gamma_c \beta + \Gamma_t (1 - \beta), \quad (\text{B12})$$

where $\beta := p_c/p$. According to Eq. (B12), Γ_1 can be considered as just the average of the cold and thermal ‘gammas’ weighted with their relative components of pressure.

The classical fundamental derivative, $\mathcal{G}_{(C)}$, for the PolyTh EoS is

$$\mathcal{G}_{(C)} = \frac{1}{2} (1 + \tilde{\Gamma}) \quad (\text{B13})$$

where

$$\tilde{\Gamma} = \frac{\Gamma_c a_c^2 + \Gamma_t a_t^2}{a_c^2 + a_t^2}, \quad (\text{B14})$$

or, alternatively

$$\tilde{\Gamma} = \frac{\Gamma_c^2 \beta + \Gamma_t^2 (1 - \beta)}{\Gamma_1}, \quad (\text{B15})$$

which can be interpreted as the ratio between the mean of both Γ_c^2 and Γ_t^2 and the adiabatic exponent Γ_1 . By construction, the quantity $\tilde{\Gamma}$ varies between the values of Γ_t and Γ_c .

The relativistic fundamental derivative, $\mathcal{G}_{(R)}$, for the PolyTh EoS is

$$\mathcal{G}_{(R)} = \mathcal{G}_{(C)} - \frac{3}{2} c_{s(R)}^2 = \frac{1}{2} (1 + \tilde{\Gamma} - 3 c_{s(R)}^2). \quad (\text{B16})$$

Some comments are in order:

1) From Eq. (B16), one concludes that the PolyTh EoS can develop, due to relativistic effects, non-convex regions there where the following relationships are satisfied:

$$\frac{1 + \tilde{\Gamma}}{3} \leq c_{s(R)}^2 \leq 1 \quad \text{and} \quad 1 \leq \tilde{\Gamma} \leq 2. \quad (\text{B17})$$

where the lower bound on $\tilde{\Gamma}$ comes from its definition, assuming that: $\Gamma_\alpha \geq 1 \quad \forall \alpha = c, t$.

2) The analysis of the particular cases $\beta = 1$ and $\beta = 0$ can shed light on the previous conclusion. These cases are easily covered by taking $\tilde{\Gamma} = \Gamma_c$ and $\tilde{\Gamma} = \Gamma_t$, respectively, in Eqs. (B13), (B16) and (B17). Let us consider, e.g. $\beta = 1$. From Eqs. (B7), (B4) and (B6) we obtain

$$i) \quad \lim_{\epsilon_c \rightarrow \infty} c_{s(R)}^2 = \Gamma_c - 1, \quad (\text{B18})$$

$$ii) \quad \lim_{\epsilon_c \rightarrow \infty} \mathcal{G}_{(R)} = 2 - \Gamma_c, \quad (\text{B19})$$

and, therefore, the thermodynamics is convex for a causal EoS, if and only if $1 \leq \Gamma_c \leq 2$, as it happens for an ideal-gas EoS.

3) The above two comments help us to give the conditions to be satisfied by the PolyTh EoS in order to be both causal and convex:

$$c_{s(R)}^2 \leq \tilde{\Gamma} - 1 \quad \text{and} \quad 1 \leq \tilde{\Gamma} \leq 2. \quad (\text{B20})$$

As an example, let us complete the analysis by taking for the PolyTh EoS one of the set of parameters used in the binary neutron star merger simulations of Maione et al. (2016), namely $\Gamma_c = 3.005$ and $\Gamma_t = 1.8$. We take ϵ_c and ϵ_t as the independent thermodynamical variables. Figure B1 shows the relativistic speed of sound, $c_{s(R)}^2$, defined in Eq. (B7). It is an increasing function, in both ϵ_c and ϵ_t , up to some value of ϵ_c^{crit} given by Eq. (B10). In our example, this

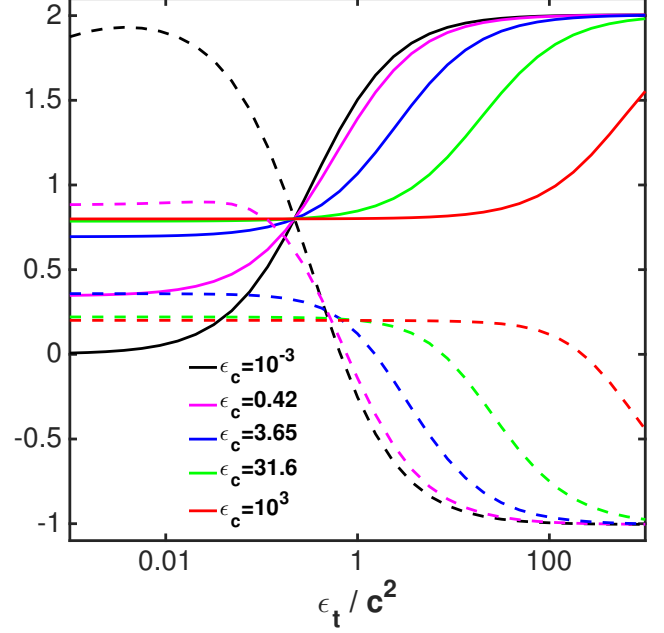


Figure B1. Relativistic fundamental derivative $\mathcal{G}_{(R)}$ in Eq. (B16) (dashed lines) and relativistic speed of sound $c_{s(R)}$ in Eq. (B7) (solid lines), versus ϵ_t , for different values of ϵ_c . We use the PolyTh EoS with $\Gamma_c = 3.005$ and $\Gamma_t = 1.8$.

value is $\epsilon_c^{\text{crit}} = 0.22$. For $\epsilon_c \geq \epsilon_c^{\text{crit}}$ (depending on ϵ_t) the PolyTh EoS becomes non-causal. On the other hand, Figure B1 also shows the relativistic fundamental derivative, $\mathcal{G}_{(R)}$, given by Eq. (B16). It is a decreasing function in both ϵ_c and ϵ_t . For $\epsilon_c \geq \epsilon_c^{\text{crit}}$ (depending on ϵ_t) the PolyTh EoS becomes non-convex.

As a summary, from the above example and from our previous analysis, we conclude that the PolyTh EoS is convex in those regions of the space of parameters in which it is causal. The non-convex regions are associated with the non-causal ones and, therefore, the corresponding subset of parameters has no physical meaning.

ACKNOWLEDGEMENTS

We gratefully acknowledge the anonymous referee for the careful examination of our work, which has greatly improved as a result of his/her feedback. We thank V. Dexheimer and S. Schramm for allowing us to use their implementation of the CMF (Λ B) EoS, since it is not included in the CompOSE database so far. We also kindly acknowledge the help of the CompOSE development team and, especially of M. Oertel. Research supported by the Spanish Ministry of Economy and Competitiveness (MINECO) through grants AYA2015-66899-C2-1-P, and MTM2014-56218-C2-2-P, and by the Generalitat Valenciana (PROMETEOII-2014-069, ACIF/2015/216). MAA acknowledges support from the European Research Council (grant CAMAP-259276). NSG and JAF acknowledge support from the European Union’s Horizon 2020 research and innovation programme under the H2020-MSCA-RISE-2017 Grant No. FunFiCO-777740. We thank the PHAROS COST Action (CA16214) and the GWverse COST Action (CA16104) for partial support. The computations were performed under grants AECT-2017-3-0007 and AECT-2018-1-0010 of the Spanish Super-

computing Network on the *MareNostrum* cluster of the Barcelona Supercomputing Centre, and on the clusters *Tirant* and *Lluïsvives* of the Servei d'Informàtica of the University of Valencia.

REFERENCES

- Abbott B. P., et al., 2016a, *Physical Review Letters*, 116, 061102
 Abbott B. P., et al., 2016b, *Physical Review Letters*, 116, 241103
 Abbott B. P., et al., 2017a, *Phys. Rev. Lett.*, 118, 221101
 Abbott B. P., et al., 2017b, *Phys. Rev. Lett.*, 119, 141101
 Abbott B. P., et al., 2017c, *Phys. Rev. Lett.*, 119, 161101
 Abbott B. P., et al., 2017d, *ApJ*, 848, L12
 Abbott B. P., et al., 2017e, *ApJ*, 848, L13
 Abbott B. P., et al., 2017f, *ApJ*, 851, L35
 Abbott B. P., et al., 2018, *Physical Review Letters*, 121, 161101
 Abdikamalov E. B., Dimmelmeier H., Rezzolla L., Miller J. C., 2009, *MNRAS*, 392, 52
 Alford M., Blaschke D., Drago A., Klähn T., Pagliara G., Schaffner-Bielich J., 2007, *Nature*, 445, 7
 Alford M. G., Han S., Prakash M., 2013, *Phys. Rev. D*, 88, 083013
 Annala E., Gorda T., Kurkela A., Vuorinen A., 2018, *Physical Review Letters*, 120, 172703
 Antoniadis J., et al., 2013, *Science*, 340, 448
 Aoki Y., Endrődi G., Fodor Z., Katz S. D., Szabó K. K., 2006, *Nature*, 443, 675
 Argrow B. M., 1996, *Shock Waves*, 6, 241
 Baiotti L., Hawke I., Montero P. J., Löffler F., Rezzolla L., Stergioulas N., Font J. A., Seidel E., 2005a, *Phys. Rev. D*, 71, 024035
 Baiotti L., Hawke I., Montero P. J., Löffler F., Rezzolla L., Stergioulas N., Font J. A., Seidel E., 2005b, *Physical Review D*, 71, 024035
 Baiotti L., Hawke I., Rezzolla L., 2007, *Classical and Quantum Gravity*, 24, S187
 Balberg S., Gal A., 1997, *Nuclear Physics A*, 625, 435
 Banik S., Hempel M., Bandyopadhyay D., 2014, *ApJS*, 214, 22
 Banyuls F., Font J. A., Ibáñez J. M. I., Martí J. M. I., Miralles J. A., 1997, *ApJ*, 476, 221
 Bardeen J. M., Thorne K. S., Meltzer D. W., 1966, *ApJ*, 145, 505
 Baumgarte T. W., Shapiro S. L., 1998, *Phys. Rev. D*, 59, 024007
 Baumgarte T. W., Montero P. J., Cordero-Carrión I., Müller E., 2013, *Phys. Rev. D*, 87, 044026
 Bauswein A., Janka H.-T., Oechslin R., 2010, *Phys. Rev. D*, 82, 084043
 Bazavov A., et al., 2014, *Phys. Rev. D*, 90, 094503
 Bedaque P., Steiner A. W., 2015, *Physical Review Letters*, 114, 031103
 Bednarek I., Haensel P., Zduunik J. L., Bejger M., Mańka R., 2012, *A&A*, 543, A157
 Bejger M., Dimmelmeier H., Haensel P., Zduunik J. L., 2012, in *Chamseddine A. H., ed., Twelfth Marcel Grossmann Meeting on General Relativity*. pp 785–787, doi:10.1142/9789814374552_0056
 Bejger M., Blaschke D., Haensel P., Zduunik J. L., Fortin M., 2017, *A&A*, 600, A39
 Bethe H., 1942, *The theory of shock waves for an arbitrary equation of state*, Tech. Paper 545, Office of Scientific Research and Development
 Bonanno L., Drago A., 2009, *Phys. Rev. C*, 79, 045801
 Borsányi S., Fodor Z., Hoellbling C., Katz S. D., Krieg S., Szabó K. K., 2014, *Physics Letters B*, 730, 99
 Brandt S. R., Seidel E., 1995, *Physical Review D*, 52, 856
 Buballa M., et al., 2014, *Journal of Physics G Nuclear Physics*, 41, 123001
 Callen H., 1985, *Thermodynamics and an Introduction to Thermostatistics*. Wiley
 Camenzind M., 2007, *Compact objects in astrophysics: white dwarfs, neutron stars, and black holes*. Springer, Berlin, Germany
 Chandrasekhar S., 1939, *An Introduction to the Stellar Structure*. Vol. 1, University of Chicago Press, Chicago, USA
 Cinnella P., 2008, *Physics of Fluids*, 20, 046103
 Cinnella P., Corre C., 2006, in *APS Division of Fluid Dynamics Meeting Abstracts*.
 Cordero-Carrión I., Cerdá-Durán P., 2012, preprint, (arXiv:1211.5930)
 Cordero-Carrión I., Cerdá-Durán P., 2014, *Advances in Differential Equations and Applications*. SEMA SIMAI Springer Series Vol. 4, Springer International Publishing Switzerland, Switzerland
 Couch S. M., O'Connor E. P., 2014, *ApJ*, 785, 123
 Couch S. M., Ott C. D., 2013, *ApJ*, 778, L7
 De S., Finstad D., Lattimer J. M., Brown D. A., Berger E., Biver C. M., 2018, *Physical Review Letters*, 121, 091102
 Demorest P. B., Pennucci T., Ransom S. M., Roberts M. S. E., Hessels J. W. T., 2010, *Nature*, 467, 1081
 Dexheimer V., Schramm S., 2008, *ApJ*, 683, 943
 Dexheimer V., Negreiros R., Schramm S., 2015, *Phys. Rev. C*, 92, 012801
 Diaz Alonso J., 1985, *Phys. Rev. D*, 31, 1315
 Dietrich T., Bernuzzi S., 2015, *Physical Review D*, 91, 044039
 Dimmelmeier H., Stergioulas N., Font J. A., 2006, *Monthly Notices of the Royal Astronomical Society*, 368, 1609
 Dimmelmeier H., Ott C. D., Marek A., Janka H.-T., 2008, *Phys. Rev. D*, 78, 064056
 Dimmelmeier H., Bejger M., Haensel P., Zduunik J. L., 2009, *Monthly Notices of the Royal Astronomical Society*, 396, 2269
 Drago A., Tambini U., 1999, *Journal of Physics G Nuclear Physics*, 25, 971
 Ducoin C., Hasnaoui K. H. O., Napolitani P., Chomaz P., Gulminelli F., 2007, *Phys. Rev. C*, 75, 065805
 Fischer T., Whitehouse S. C., Mezzacappa A., Thielemann F. K., Liebendörfer M., 2010, *A&A*, 517, A80
 Fischer T., et al., 2011, *ApJS*, 194, 39
 Fischer T., et al., 2018, *Nature Astronomy*, 2, 980
 Font J. A., et al., 2002a, *Phys. Rev. D*, 65, 084024
 Font J. A., et al., 2002b, *Physical Review D*, 65, 084024
 Giacomazzo B., Perna R., 2012, *ApJ*, 758, L8
 Giacomazzo B., Rezzolla L., Stergioulas N., 2011, *Phys. Rev. D*, 84, 024022
 Glendenning N. K., 2000, *Compact stars: nuclear physics, particle physics, and general relativity*. Springer, New York, USA
 Glendenning N. K., 2001, *Phys. Rep.*, 342, 393
 Glendenning N. K., Kettner C., 2000, *A&A*, 353, L9
 Guardone A., Vigevano L., 2002, *Journal of Computational Physics*, 175, 50
 Guardone A., Zamfirescu C., Colonna P., 2010, *Journal of Fluid Mechanics*, 642, 127
 Guilet J., Müller E., Janka H.-T., 2015, *MNRAS*, 447, 3992
 Guilet J., Müller E., Janka H.-T., Rembiasz T., Obergaullinger M., Cerdá-Durán P., Aloy M.-A., 2017, in *Marcowith A., Renaud M., Dubner G., Ray A., Bykov A., eds, IAU Symposium Vol. 331, Supernova 1987A:30 years later - Cosmic Rays and Nuclei from Supernovae and their Aftermaths*. pp 119–124 (arXiv:1706.08733), doi:10.1017/S1743921317004732
 Gulminelli F., Raduta A. R., Oertel M., Margueron J., 2013, *Phys. Rev. C*, 87, 055809
 Haensel P., Potekhin A. Y., 2004, *A&A*, 428, 191
 Haensel P., Levenfish K. P., Yakovlev D. G., 2002, *A&A*, 394, 213
 Haensel P., Potekhin A. Y., Yakovlev D. G., eds, 2007, *Neutron Stars I: Equation of State and Structure Astrophysics and Space Science Library Vol. 326*. New York: Springer
 Heiselberg H., Hjorth-Jensen M., 2000, *Phys. Rep.*, 328, 237
 Hempel M., Schaffner-Bielich J., 2010, *Nuclear Physics A*, 837, 210
 Hempel M., Fischer T., Schaffner-Bielich J., Liebendörfer M., 2012, *ApJ*, 748, 70
 Hempel M., Dexheimer V., Schramm S., Iosilevskiy I., 2013, *Phys. Rev. C*, 88, 014906
 Ibáñez J. M., Cordero-Carrión I., Martí J. M., Miralles J. A., 2013, *Classical and Quantum Gravity*, 30, 057002
 Ibáñez J. M., Marquina A., Serna S., Aloy M. A., 2018, *MNRAS*, 476, 1100
 Iosilevskiy I., 2010, *Acta Phys. Polon. B (Proc. Supl.)*, 3, 589
 Janka H.-T., Hanke F., Hüdephol L., Marek A., Müller B., Obergaullinger M., 2012, *Progress of Theoretical and Experimental Physics*, 2012, 01A309

- Lalazissis G. A., König J., Ring P., 1997, *Phys. Rev. C*, 55, 540
- Lattimer J. M., Swesty F. D., 1991, *Nuclear Physics A*, 535, 331
- Maione F., De Pietri R., Feo A., Löffler F., 2016, *Classical and Quantum Gravity*, 33, 175009
- Malik T., Alam N., Fortin M., Providência C., Agrawal B. K., Jha T. K., Kumar B., Patra S. K., 2018, *Phys. Rev. C*, 98, 035804
- Marek A., Dimmelmeier H., Janka H.-T., Müller E., Buras R., 2006, *A&A*, 445, 273
- Margalit B., Metzger B. D., 2017, *ApJ*, 850, L19
- Marques M., Oertel M., Hempel M., Novak J., 2017, *Phys. Rev. C*, 96, 045806
- Martí J. M., Miralles J. A., Ibanez J. M., Diaz Alonso J., 1988, *ApJ*, 329, 780
- Menikoff R., Plohr B. J., 1989, *Reviews of Modern Physics*, 61, 75
- Montero P. J., Cordero-Carrion I., 2012, *Phys.Rev.*, D85, 124037
- Montero P. J., Baumgarte T. W., Müller E., 2014, *Phys. Rev. D*, 89, 084043
- Most E. R., Papenfort L. J., Dexheimer V., Hanauske M., Schramm S., Stöcker H., Rezzolla L., 2018a, arXiv e-prints,
- Most E. R., Weih L. R., Rezzolla L., Schaffner-Bielich J., 2018b, *Physical Review Letters*, 120, 261103
- Müller E., Eriguchi Y., 1985, *A&A*, 152, 325
- Nakazato K., Sumiyoshi K., Yamada S., 2008, *Phys. Rev. D*, 77, 103006
- Nandi R., Schramm S., 2017, *Phys. Rev. C*, 95, 065801
- Newman E., Penrose R., 1962, *Journal of Mathematical Physics*, 3, 566
- O'Connor E., Ott C. D., 2010, *Classical and Quantum Gravity*, 27, 114103
- O'Connor E., Ott C. D., 2011, *ApJ*, 730, 70
- Obergaulinger M., Aloy M. Á., 2017, *MNRAS*, 469, L43
- Obergaulinger M., Janka H.-T., Aloy M. A., 2014, *MNRAS*, 445, 3169
- Obergaulinger M., Just O., Aloy M. Á., 2018, *Journal of Physics G*, 45, 084001
- Oertel M., Fantina A. F., Novak J., 2012, *Phys. Rev. C*, 85, 055806
- Pais H., Newton W. G., Stone J. R., 2014, *Phys. Rev. C*, 90, 065802
- Peres B., 2013, PhD thesis, University of Paris VII
- Peres B., Oertel M., Novak J., 2013a, *Phys. Rev. D*, 87, 043006
- Peres B., Oertel M., Novak J., 2013b, *Phys. Rev. D*, 87, 043006
- Pons J. A., 1999, PhD thesis, University of Valencia
- Pons J. A., Reddy S., Prakash M., Lattimer J. M., Miralles J. A., 1999, *ApJ*, 513, 780
- Radice D., Perego A., Zappa F., Bernuzzi S., 2018, *ApJ*, 852, L29
- Raduta A. R., Gulminelli F., 2010, *Phys. Rev. C*, 82, 065801
- Raithel C. A., Özel F., Psaltis D., 2018, *ApJ*, 857, L23
- Sagert I., Fischer T., Hempel M., Pagliara G., Schaffner-Bielich J., Mezzacappa A., Thielemann F.-K., Liebendörfer M., 2009, *Physical Review Letters*, 102, 081101
- Sagert I., Fischer T., Hempel M., Pagliara G., Schaffner-Bielich J., Thielemann F.-K., Liebendörfer M., 2010, *Journal of Physics G Nuclear Physics*, 37, 094064
- Sanchis-Gual N., Degollado J. C., Montero P. J., Font J. A., Mewes V., 2015, *Phys. Rev. D*, 92, 083001
- Sanchis-Gual N., Herdeiro C., Radu E., Degollado J. C., Font J. A., 2017, *Phys. Rev. D*, 95, 104028
- Schertler K., Greiner C., Schaffner-Bielich J., Thoma M. H., 2000, *Nuclear Physics A*, 677, 463
- Schürhoff T., Schramm S., Dexheimer V., 2010, *ApJ*, 724, L74
- Serna S., Marquina A., 2014, *Physics of Fluids*, 26, 016101
- Shapiro S. L., Teukolsky S. A., 1983, *Black holes, white dwarfs, and neutron stars: The physics of compact objects*. Wiley-Interscience
- Shen H., Toki H., Oyamatsu K., Sumiyoshi K., 1998a, *Progress of Theoretical Physics*, 100, 1013
- Shen H., Toki H., Oyamatsu K., Sumiyoshi K., 1998b, *Nuclear Physics A*, 637, 435
- Shen G., Horowitz C. J., Teige S., 2011a, *Phys. Rev. C*, 83, 035802
- Shen G., Horowitz C. J., O'Connor E., 2011b, *Phys. Rev. C*, 83, 065808
- Shibata M., Nakamura T., 1995, *Phys. Rev. D*, 52, 5428
- Steiner A., Fischer T., Gandolfi S., Hempel M., 2012, in *Nuclei in the Cosmos (NIC XII)*. p. 38
- Stergioulas N., Friedman J. L., 1995, *ApJ*, 444, 306
- Stergioulas N., Apostolatos T. A., Font J. A., 2004, *Monthly Notices of the Royal Astronomical Society*, 352, 1089
- Sugahara Y., Toki H., 1994, *Nuclear Physics A*, 579, 557
- Sumiyoshi K., Yamada S., Suzuki H., Shen H., Chiba S., Toki H., 2005, *ApJ*, 629, 922
- Suwa Y., 2014, *Publications of the Astronomical Society of Japan*, 66, L1
- Thompson P. A., 1971, *Physics of Fluids*, 14, 1843
- Thompson P. A., Kim Y. G., Carofano G. C., 1986, *Journal of Fluid Mechanics (ISSN 0022-1120)*, 166, 57
- Thorne K. S., 1980, *Reviews of Modern Physics*, 52, 299
- Todd-Rutel B. G., Piekarewicz J., 2005, *Physical Review Letters*, 95, 122501
- Toki H., Hirata D., Sugahara Y., Sumiyoshi K., Tanihata I., 1995, *Nuclear Physics A*, 588, 357
- Typel S., Röpke G., Klähn T., Blaschke D., Wolter H. H., 2010, *Phys. Rev. C*, 81, 015803
- Vaidya B., Mignone A., Bodo G., Massaglia S., 2015, *A&A*, 580, A110
- Voss A., 2005, PhD thesis, University of Wuppertal
- Weber F., 2005, *Progress in Particle and Nuclear Physics*, 54, 193
- Woosley S. E., Heger A., 2007, *Phys. Rep.*, 442, 269
- Zdunik J. L., Haensel P., 2013, *A&A*, 551, A61
- Zel'dovich Y., 1946, *Zh. Eksp. Teor. Fiz.*, 4, 363
- Zhou E.-P., Zhou X., Li A., 2018, *Phys. Rev. D*, 97, 083015
- van Riper K. A., 1978, *ApJ*, 221, 304